Gyrokinetic Analysis of Ion Temperature Gradient Modes in Helical Systems

–ヘリカル系におけるイオン温度勾配モードのジャイロ運動論的解析–

黒田 徹

Tohru Kuroda

総合研究大学院大学 数物科学研究科 核融合科学専攻

Department of Fusion Science

School of Mathematical and Physical Science

The Graduate University for Advanced Studies

平成十二年三月

March, 2000

Abstract

The ion temperature gradient (ITG) mode is one of drift wave instabilities, which is considered to cause the anomalous transport of the ion thermal energy in high temperature plasmas. The purpose of this thesis is to clarify effects of magnetic configurations on the ITG mode based on the gyrokinetic model. The gyrokinetic equation for ions is used to consider kinetic effects such as finite gyroradii and wave-pariticle interactions. Also, the assumption of adiabatic electrons and the quasineutrality condition are used to obtain the dispersion relation. Phase mixing due to ∇B-curvature drift motion is investigated in detail in the local approximation. Effects of magnetic configuration on nonlocal mode structure are studied in straight and toroidal helical systems.

In the local approximation, initial value problem of the ITG mode is solved. Due to the toroidal magnetic drift, the Laplace-transformed density and potential perturbations have a branch cut as well as poles on the complex-frequency plane. The inverse Laplace transform shows that the temporal evolution of the density and potential perturbations consists of the normal modes and the continuum mode, which correspond to contributions from the poles and the branch cut, respectively. The normal modes have exponential time dependence with the eigenfrequencies determined by the dispersion relation while the continuum mode shows power-law decay oscillation. For the stable case, the long-time asymptotic behavior of the potential and density perturbations is dominated by the continuum mode which decays slower than the normal modes.

Next, poloidal localization of the mode structure is studied by means of the ballooning representation. In the first place, the straight helical system is considered in order to focus on the helical ripples' effects. The magnetic shear is assumed to be negative and the poloidal period number L is taken as $L = 2$. Then, the helical ripples with a larger toroidal period number M reduce the growth rate of the ITG mode. This stabilizing effect is understood based on the structure of the eigenfunction along the field line as follows. As M increases, the connection length between the good and bad curvature regions becomes shorter and the eigenfunction enters the good curvature region, which leads to the stabilization. For large M ($M \sim 10$), unstable ITG modes are driven only by the very large temperature gradients.

Finally, toroidal helical systems are considered, in which toroidicity and helical ripples exist simultaneously. Equilibrium plasma parameters are chosen in reference to the LHD experimental result($L = 2$, $M = 10$). Because of the toroidal destabilization, the critical temperature gradient in which ITG mode becomes unstable is smaller than for the straight helical system. Numerical results suggest the existence of unstable ITG modes in LHD. The good curvature region is generated even in the outer torus region due to the helical ripples, which results in the reduction of growth rate compared to the tokamak cases without helical ripples. Also, dependences of the ITG mode properties on various plasma equilibrium parameters such as the helical ripple intensity, safety factor, magnetic shear, ballooning angle, poloidal wavenumber, temperature and density gradients are investigated.

Contents

Chapter 1

Introduction

Magnetic Plasma Confinement is one of the means to realize controlled nuclear fusion. Macroscopic behaviors of a plasma in a magnetic toroid are well described by the magnetohydrodynamics (MHD) [1]. The MHD theory is extensively utilized to design favorable magnetic configurations, in which stable plasma equilibria are sustained. Even if a plasma is MHD-stable (or macroscopically stable), plasma particles and heat leak out in diffusive process, which is a subject of transport theories. The classical and neoclassical transport theories [2, 3, 4, 5] are a well-established framework which explains particles' scattering processes due to the Coulomb collisions. However, particle and heat fluxes observed in fusion plasma experiments are significantly larger than those predicted by the collisional (classical and neoclassical) transport theories and are called the anomalous transport [6]. The anomalous transport is generally believed to result from fluctuations (or turbulence) driven by various microinstabilities, which exist in inhomogeneous plasmas. The ion temperature gradient (ITG) mode is one of drift wave instabilities [7], on which many works have been done as a cause of the anomalous ion heat transport in high temperature core regions of tokamak plasmas [8].

It is well-known that there are two branches of the ITG mode: the slab ITG mode and the toroidal ITG mode [9]. Simple derivation of the dispersion relation for the slab and

toroidal ITG modes can be done by the fluid description, which is valid for waves with long wavelengths and higher phase velocities than the particles' thermal velocity. Then, the slab ITG mode arises as the drift-acoustic wave branch and its growth rate is roughly given by $\gamma_{max} = (k_{\|}^2 c_s^2 \omega_{*pi})^{1/3}$, where $k_{\|}$ is the parallel wavenumber, $C_s = (T_e/m_i)^{1/2}$ is the sound velocity and $\omega_{*pi} = (k_y c/e_i B n_i)(dp_i/dx)$ is the ion pressure gradient drift frequency. The toroidal ITG mode is driven by the ion ∇B-curvature drift motion combined with the ion temperature gradient, and its growth rate is written as $\gamma_{max} = \sqrt{\omega_{*pi}\omega_{Di}/(1+k_\perp^2\rho_s^2)}$, where $\omega_{Di} = (2k_y c T_i)/(e_i B R)$ is the ion toroidal drift frequency. Because of its larger growth rate, most recent studies are concerned with the toroidal ITG mode.

Recently, the Large Helical Device (LHD) [10, 11, 12, 13, 14] of National Institute for Fusion Science succeeded in generation of the high ion temperature $T_i \geq 3$ keV by means of neutral beam injection [15]. Observed ion temperature profiles are steeper than density profiles. Thus, the ITG modes are expected to become unstable and drive the anomalous transport in helical systems as well.

The purpose of this thesis is to investigate the linear properties of the ITG mode in toroidal systems including helical devices. In order to accurately estimate the ITG mode properties (the real frequency, growth rate and mode structure), we need to take account of kinetic effects such as finite gyroradii and wave-particle interactions. For that purpose, we describe the ion dynamics based on the gyrokinetic equation in which the magnetic configuration effects are included through the ion ∇B-curvature drift velocity.

This thesis is organized as follows. In Chapter 2, the initial value problem of the toroidal ion temperature gradient mode is studied based on the Laplace transform of the ion gyrokinetic equation and the electron Boltzmann relation with the charge neutrality condition. Due to the toroidal magnetic drift, the Laplace-transformed density and potential perturbations have a branch cut as well as poles on the complex-frequency plane. The inverse Laplace transform shows that the temporal evolution of the density and potential perturbations consists of the normal modes and the continuum mode, which correspond to

contributions from the poles and the branch cut, respectively. The normal modes have exponential time dependence with the eigenfrequencies determined by the dispersion relation while the continuum mode shows power-law decay oscillation. For the stable case, the long-time asymptotic behavior of the potential and density perturbations is dominated by the continuum mode which decays slower than the normal modes.

In Chapter 3, ion temperature gradient (ITG) modes in helical systems are studied. The gyrokinetic equation for ions, the adiabatic assumption for electrons, and the charge neutrality condition are used with the ballooning representation to derive a kinetic integral equation, which is solved numerically to obtain the linear growth rate, the real frequency, and the eigenfunction of the ITG modes. Using a simple helical field model, cases with $L = 2$ and $2 \leq M \leq 10$ are investigated where L and M are the poloidal and toroidal polarity numbers characterizing the helical field ripple, respectively. The effects of the toroidal polarity number M on the dispersion relation and the mode structure of the ITG modes are clarified.

In Chapter 4, linear properties of ion temperature gradient (ITG) modes in helical systems are studied. The real frequency, growth rate, and eigenfunction are obtained for both stable and unstable cases by solving a kinetic integral equation with proper analytic continuation performed in the complex frequency plane. Based on the model magnetic configuration for toroidal helical systems like the Large Helical Device (LHD), dependences of the ITG mode properties on various plasma equilibrium parameters are investigated. Particularly, relative effects of ∇B-curvature drifts driven by the toroidicity and by the helical ripples are examined in order to compare the ITG modes in helical systems with those in tokamaks.

Finally, the main results obtained in this thesis are summarized in Chapter 5.

Chapter 2

Local Analysis of ITG Modes

2.1 Introduction

Many works have been done on the ion temperature gradient mode (ITG mode) [8, 16, 17, 18, 19, 20, 21, 22, 23, 24, 25] because it is considered as the most likely instability to cause the anomalous ion thermal transport observed in high ion temperature plasmas. It is well-known that there are two branches of the ITG mode: the slab ITG mode and the toroidal ITG mode [9]. Because of its larger growth rate, in the present study as in most recent works, we are concerned with the toroidal ITG mode which is driven by the ion temperature gradient combined with the toroidal magnetic ∇B-curvature drift.

The kinetic dispersion relation for the toroidal ITG mode including effects of the finite gyroradius and the toroidal resonance are derived by using the gyrokinetic equation [26, 27] for ions and the Boltzmann distribution for electrons with the charge neutrality condition. Due to the quadratic form of the parallel and perpendicular velocities in the ∇B-curvature drift, the toroidal resonance has qualitatively different characteristics from the parallel drift resonance in the slab case. Thus, when we define the dispersion function on the complex-frequency ω-plane for the toroidal ITG mode, its analytic continuation requires a branch cut on the $\mathrm{Im}(\omega) < 0$ plane [28, 29]. We need to take account of this property caused

by the toroidal resonance in order to obtain the complex eigenfrequencies especially with negative imaginary parts (or negative growth rates) from the dispersion relation [29]. These eigenfrequencies ω determine the temporal behavior of the normal modes as $\propto \exp(-\mathrm{i}\omega t)$. However, as shown by Kim *et al.* [29], the ballistic response in the presence of the toroidal resonance shows a slow power-law decay rather than the exponential decay of stable normal modes. Therefore, description of the toroidal ITG mode only by the normal modes seems to be incomplete especially for stable systems. The power-law decay oscillation may be called continuum modes which are required for the complete representation of the initial value problem.

In this chapter, we direct our attention to rigorous description of temporal evolution of the toroidal ITG mode including both exponential and power-law dependence. For that purpose, the initial value problem of the toroidal ITG mode is explicitly formulated based on the Laplace transform with respect to time. We also use the local approximation to consider the stability for the Fourier component with specified parallel and perpendicular wavenumbers. We treat appropriately a Landau contour and a branch cut for analytic continuation on the complex ω-plane by following Kim *et al.* [29]. Then, we show that the density and potential perturbations of the toroidal ITG mode contain two different types of temporal behavior: the normal modes and the continuum mode which correspond to contributions from the poles and the branch cut of the Laplace-transformed potential function on the complex ω-plane, respectively. The continuum mode is shown to decay by power law like the ballistic response and dominates the asymptotic behavior of the toroidal ITG mode for the stable case.

This work is organized as follows. In § 2.2, the ion gyrokinetic equation and its Laplace transform are presented. The ballistic response is derived from the propagator in the gyrokinetic equation, and the density perturbation decay due to the phase mixing by the parallel and toroidal drift is shown. In § 2.3, the toroidal ITG mode is formulated as an initial value problem. Analytic continuation on the complex-frequency plane for the

case with the toroidal magnetic drift is reviewed. Temporal evolution of the density and potential perturbations of the toroidal ITG mode is shown to consist of the normal modes and the continuum mode. In § 2.4, the dispersion relation and the initial value problem of the ITG mode are numerically solved to show the behavior of the normal and continuum modes in some examples. Finally, conclusions are given in § 2.5. These works are published in [30].

2.2 Ion Gyrokinetic Equation

2.2.1 Laplace transform of the gyrokinetic equation

The ion distribution function in the $(\boldsymbol{x}, \boldsymbol{v})$ phase space is divided into the equilibrium and perturbation parts as $f_i = n_0 F_M + \delta f_i$ where n_0 is the equilibrium density, $F_M \equiv \pi^{-3/2} v_{Ti}^{-3} \exp(-v^2/v_{Ti}^2)$ is the Maxwellian distribution function, and $v_{Ti} \equiv (2T_i/m_i)^{1/2}$ is the thermal velocity for the ions with the mass m_i, the temperature T_i, and the electric charge e. In the magnetic field $\boldsymbol{B}$, the perturbation part δf_i with the perpendicular wavenumber vector $\boldsymbol{k}_\perp$ is written as

$$\delta f_i = -\frac{e\phi}{T_i} n_0 F_M + h\, \mathrm{e}^{-\mathrm{i}\boldsymbol{k}_\perp \cdot \boldsymbol{\rho}} \tag{2.1}$$

where ϕ represents the electrostatic potential, $\boldsymbol{\rho} \equiv \boldsymbol{b} \times \boldsymbol{v}/\Omega_i$ $(\boldsymbol{b} = \boldsymbol{B}/B)$ denotes the ion gyroradius vector, and $\Omega_i \equiv eB/(m_i c)$ is the ion gyrofrequency. Here, the first and second terms in the right-hand side of eq. (2.1) represents the adiabatic and nonadiabatic parts, respectively. The velocity vector $\boldsymbol{v}$ is written as $\boldsymbol{v} = v_\parallel \boldsymbol{b} + v_\perp(\boldsymbol{e}_1 \cos\xi + \boldsymbol{e}_2 \sin\xi)$ where ξ is the gyrophase and $(\boldsymbol{e}_1, \boldsymbol{e}_2, \boldsymbol{b})$ are the unit vectors which forms a right-hand orthogonal system at each point. The ion nonadiabatic distribution function h is independent of the gyrophase and is described in the linear, collisionless, and electrostatic case by the gyrokinetic equation [26, 27] as

$$\left(\frac{\partial}{\partial t} + \mathrm{i}\omega_D + \mathrm{i}k_\parallel v_\parallel\right) h = \left(\frac{\partial}{\partial t} + \mathrm{i}\omega_{*T}\right) \frac{e\phi}{T_i} J_0(k_\perp \rho)\, n_0 F_M \tag{2.2}$$

where J_0 is the Bessel function of order zero, $\omega_D \equiv \hat{\omega}_D(v_\perp^2/2 + v_\parallel^2)/v_{Ti}^2$ is the ion ∇B-curvature drift frequency, and $\omega_{*T} = \omega_{*i}[1 + \eta_i\{(v/v_{Ti})^2 - 3/2\}]$. The characteristic ion ∇B-curvature drift frequency is given by $\hat{\omega}_D \equiv 2\epsilon_n\omega_{*i}$ where $\omega_{*i} \equiv -\tau_e^{-1}\omega_{*e}$ is the ion diamagnetic drift frequency and $\epsilon_n \equiv L_n/R$ is the ratio of the equilibrium density gradient scale length $L_n \equiv -(d\ln n_0/dr)^{-1}$ to the magnetic curvature radius R. Here $\tau_e \equiv T_e/T_i$ is the ratio between the electron and ion temperatures, $\omega_{*e} \equiv ck_\theta T_e/(eBL_n)$ is the electron diamagnetic drift frequency, and k_θ is the poloidal wavenumber. The ratio of the ion temperature gradient to the density gradient is given by $\eta_i \equiv d\ln T_i/d\ln n_0$. In the gyrokinetic equation eq. (2.2), we have used the local kinetic approximation to replace the parallel drift operator $v_\parallel \boldsymbol{b}\cdot\nabla$ with $\mathrm{i}k_\parallel v_\parallel$ in terms of the parallel wavenumber $k_\parallel$. Here we assume that the perturbation is localized in the bad curvature region of the magnetic confinement system and, in the case of tokamaks, the ∇B-curvature drift frequency $\hat{\omega}_D \equiv 2\epsilon_n\omega_{*i}$ corresponds to the value at the outermost point of the magnetic field line on the toroidal surface. Using this local approximation for the toroidal system with a large aspect ratio, the perpendicular wavenumber is approximately given by the poloidal wavenumber as $k_\perp \simeq k_\theta$.

In order to treat the initial value problem, it is convenient to introduce the Laplace transform

$$h(\omega) = \int_0^\infty dt\, h(t)\mathrm{e}^{\mathrm{i}\omega t} \tag{2.3}$$

and rewrite eq. (2.2) as

$$h(\omega) = \frac{\omega - \omega_{*T}}{\omega - \omega_D - k_\parallel v_\parallel}\frac{e\phi}{T_i}J_0 n_0 F_M + \mathrm{i}\frac{\langle\, \delta f_i(t=0)\, \mathrm{e}^{\mathrm{i}\boldsymbol{k}_\perp\cdot\boldsymbol{\rho}}\,\rangle}{\omega - \omega_D - k_\parallel v_\parallel} \tag{2.4}$$

where $\langle\cdots\rangle$ denotes the gyrophase average.

2.2.2 Ballistic response

Here we consider the ballistic response to the initial perturbation in the presence of the toroidal resonance, which is determined by the propagator in the left-hand side of the gyrokinetic equation eq. (2.2). The same problem was already treated by Kim *et al.* [29].

although it is reviewed here for comparison to the full initial value problem of the toroidal ITG mode shown later. Let us put $\phi = 0$ to neglect the right-hand side of the gyrokinetic equation eq. (2.2). Then, from the inverse Laplace transform of eq. (2.4) or directly from eq. (2.2) with $\phi = 0$, we obtain

$$\begin{aligned} h(t) &= \mathrm{i} \int_C \frac{d\omega}{2\pi} \frac{h(t=0)\, \mathrm{e}^{-\mathrm{i}\omega t}}{\omega - \omega_D - k_\parallel v_\parallel} \\ &= h(t=0)\ \exp[\, -\mathrm{i}(\omega_D + k_\parallel v_\parallel)\, t\,]. \end{aligned} \tag{2.5}$$

The ion density perturbation is given by

$$\begin{aligned} \delta n_i(t) &= \int d^3v\ J_0(k_\perp \rho)\ h(t) \\ &= \mathrm{i} \int_L \frac{d\omega}{2\pi} \int d^3v\ \frac{J_0(k_\perp \rho)\ h(t=0)\ \mathrm{e}^{-\mathrm{i}\omega t}}{\omega - \omega_D - k_\parallel v_\parallel} \\ &= \int d^3v\ J_0(k_\perp \rho)\ h(t=0)\ \exp[-\mathrm{i}(\omega_D + k_\parallel v_\parallel) t]. \end{aligned} \tag{2.6}$$

We find in the next section how to take the contours C and L in eqs. (2.5) and (2.6).

Here, we assume the initial condition to be given by

$$h(t=0) = C_h\ J_0(k_\perp \rho)\ F_M \tag{2.7}$$

where C_h is a constant. The above form is taken in order to simplify comparison to the case of the initial value problem including self-consistent potential fluctuations considered in the next section. Then we obtain from eqs. (2.6) and (2.7),

$$\frac{\delta n(t)}{\delta n(0)} = \frac{\Gamma_0[b_i/(1 + \mathrm{i}\hat{\omega}_D t/2)]}{\Gamma_0(b_i)} \frac{\exp[-k_\parallel^2 v_{Ti}^2 t^2/4(1 + \mathrm{i}\hat{\omega}_D t)]}{(1 + \mathrm{i}\hat{\omega}_D t/2)(1 + \mathrm{i}\hat{\omega}_D t)^{1/2}} \tag{2.8}$$

where $b_i = k_\perp^2 \rho_{Ti}^2/2$, $\rho_{Ti}^2 = v_{Ti}^2/\Omega_i^2 = 2c^2 m_i T_i/(e^2 B^2)$, $\Gamma_0(b_i) = I_0(b_i)\exp(-b_i)$, and I_0 is the modified Bessel function of order zero. In the limit of $k_\perp \rho_{Ti} \to +0$, we have $\Gamma_0 \to 1$ and eq. (2.8) reduces to the result obtained by Kim *et al.* [29]. The temporal dependence

of the density perturbation $\delta n(t)$ divides into two limiting cases as

$$\frac{\delta n(t)}{\delta n(0)} = \begin{cases} \exp(-{k_\parallel}^2 v_{Ti}^2 t^2/4) \\ \text{for } |\hat{\omega}_D t| < 1 \\ \\ \dfrac{2\ \exp\left[-k_\parallel^2 v_{Ti}^2/(4\hat{\omega}_D^2)\right] \exp\left[\mathrm{i} k_\parallel^2 v_{Ti}^2 t/(4\hat{\omega}_D)\right]}{\Gamma_0(b_i)(\mathrm{i}\hat{\omega}_D t)^{3/2}} \\ \\ \text{for } |\hat{\omega}_D t| > 1. \end{cases} \tag{2.9}$$

For $|\hat{\omega}_D t| < 1$, the density perturbation decays exponentially due to the phase mixing by the parallel drift provided $|k_\parallel v_{Ti}| > 2|\hat{\omega}_D|$. On the other hand, for $|\hat{\omega}_D t| > 1$, the phase mixing is dominated by the toroidal magnetic ∇B-curvature drift and the density perturbation decays according to the power law $\propto t^{-3/2}$ with oscillation at the frequency $\omega_{br} = -k_\parallel^2 v_{Ti}^2/(4\hat{\omega}_D)$ which we call the branch frequency.

2.3 Time Evolution of the Toroidal ITG Mode

2.3.1 Formulation of the toroidal ITG mode as an initial value problem

In order to describe the toroidal ITG mode as an initial value problem, we use the Laplace-transformed ion gyrokinetic equation eq. (2.4). Furthermore, assuming the electron density perturbation δn_e to satisfy the Boltzmann relation

$$\frac{\delta n_e}{n_0} = \frac{e\phi}{T_e} \tag{2.10}$$

and using the charge neutrality condition

$$\delta n_e = \delta n_i \tag{2.11}$$

we obtain

$$\frac{e\phi(\omega)}{T_i} = \frac{I(\omega)}{D(\omega)} \tag{2.12}$$

where

$$I(\omega) = \int d^3v \frac{\mathrm{i} J_0(k_\perp \rho) \langle\, n_0^{-1} \delta f_i(t=0)\, \mathrm{e}^{\mathrm{i}\boldsymbol{k}_\perp \cdot \boldsymbol{\rho}} \,\rangle}{\omega - \omega_D - k_\parallel v_\parallel} \tag{2.13}$$

$$D(\omega) = 1 + \tau_e^{-1} - \int d^3v \frac{(\omega - \omega_{*T})\, J_0^2(k_\perp \rho) F_M}{\omega - \omega_D - k_\parallel v_\parallel}. \tag{2.14}$$

The dispersion relation for the toroidal ITG mode with $\boldsymbol{k} = k_\parallel \boldsymbol{b} + \boldsymbol{k}_\perp$ is given by $D(\omega) = 0$. The time evolution of the electrostatic potential is given by the inverse Laplace transform of $\phi(\omega)$ in eq. (2.12) as

$$\phi(t) = \int_L \frac{d\omega}{2\pi} \phi(\omega)\, \mathrm{e}^{-\mathrm{i}\omega t} \tag{2.15}$$

where L is a contour which lies above all of the singular points of $\phi(\omega)$ on the complex ω plane. Also, substituting eq. (2.12) into eq. (2.4) and taking its inverse Laplace transform, we can obtain the time evolution of the nonadiabatic distribution function $h(t)$.

2.3.2 Analytic continuation on the complex-frequency plane

In order to obtain $\phi(\omega)$ for any complex-valued frequency ω, we need to evaluate analytical continuation of the functions $I(\omega)$ and $D(\omega)$ accurately. For that purpose, we follow Kim *et al.* [29] and consider the velocity-space integral in the form of

$$P(\omega) = \int_{-\infty}^{\infty} dv_\parallel \int_0^\infty v_\perp dv_\perp \frac{g(\omega, v_\parallel, v_\perp)}{\omega + a{v_\perp}^2 + b{v_\parallel}^2 - c v_\parallel} \tag{2.16}$$

where a, b, and c are assumed to be real constants. The functions $D(\omega)$ and $I(\omega)$ both contain the same form of functions as $P(\omega)$. Also assuming a and b to be positive, we transform the velocity-space variables as

$$v_\perp' = \sqrt{a} v_\perp \quad {v_\parallel}' = \sqrt{b}\left(v_\parallel - \frac{c}{2b}\right) \tag{2.17}$$

and

$$v' = \sqrt{({v_\perp}')^2 + ({v_\parallel}')^2}, \quad \mu = v_\parallel'/v'. \tag{2.18}$$

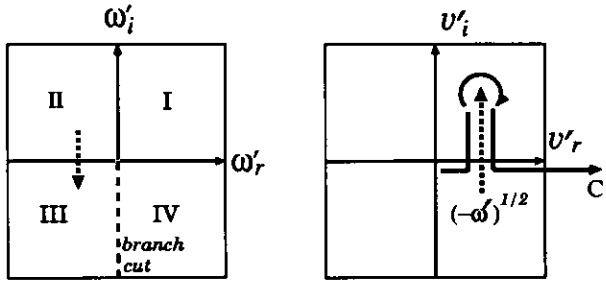

Fig. 1(a) Fig. 1(b)

Figure 2.1: Motions of the complex frequency $\omega' = \omega - c^2/4b$ on the complex ω'-plane (a) and the corresponding pole $(-\omega')^{1/2}$ with $\mathrm{Re}(-\omega')^{1/2} > 0$ in the complex v'-plane (b). When ω' moves from $\omega_i' = \mathrm{Im}(\omega') > 0$ to $\omega_i' < 0$ across the ω_r'-axis with $\omega_r' = \mathrm{Re}(\omega') < 0$, the pole $(-\omega')^{1/2}$ with $\mathrm{Re}(-\omega')^{1/2} > 0$ crosses the v_r'-axis with $v_r' = \mathrm{Re}(v') > 0$. A branch cut is taken from $\omega' = 0$ along the ω_i'-axis with $\omega_i' < 0$ as shown by a dashed line in (a).

Then, the function $P(\omega)$ is rewritten as

$$P(\omega) = \frac{1}{a\sqrt{b}} \int_{-1}^{1} d\mu \int_{0}^{\infty} v'^2 dv' \, \frac{G(\omega, v', \mu)}{\omega' + v'^2} \tag{2.19}$$

where we have defined $\omega' = \omega - c^2/4b$ and $G(\omega, v', \mu) = g[\omega, v_{\|}(v', \mu), v_{\perp}(v', \mu)]$ with $v_{\|}(v', \mu)$ and $v_{\perp}(v', \mu)$ given by the relations in eqs. (2.17) and (2.18). Apparently, the integrand has two poles $v' = \pm(-\omega')^{1/2}$ on the complex v'-plane. When ω' moves from $\omega_i' = \mathrm{Im}(\omega') > 0$ to $\omega_i' < 0$ across the ω_r'-axis with $\omega_r' = \mathrm{Re}(\omega') < 0$, one of these poles $(-\omega')^{1/2}$ with $\mathrm{Re}(-\omega')^{1/2} > 0$ crosses the v_r'-axis with $v_r' = \mathrm{Re}(v') > 0$, which corresponds to the occurrence of resonant particles. These motions of ω' and a corresponding pole $(-\omega')^{1/2}$ with $\mathrm{Re}(-\omega')^{1/2} > 0$ on the complex v'-plane are shown in Figs. 2.1 (a) and (b), respectively. This crossing requires the residue of the integrand at the pole to be included in $P(\omega)$ for its analytic continuation as shown in Fig. 2.1 (b).

On the other hand, when ω' moves from $\omega_i' > 0$ to $\omega_i' < 0$ across the ω_r'-axis with $\omega_r' > 0$,

the two poles neither cross the v'_r-axis nor make any residue's contributions to $P(\omega)$. Then, we make a branch cut from $\omega' = 0$ along the ω'_i-axis with $\omega'_i < 0$ as shown in Fig. 2.1 (a) and write $P(\omega)$ as

$$P(\omega) = \begin{cases} P_0(\omega) & \text{in I, II, and IV} \\ P_0(\omega) + \Delta_P(\omega) & \text{in III} \end{cases} \tag{2.20}$$

where I–IV represent the regions on the complex ω'-plane shown by Fig. 2.1 (a) and $P_0(\omega)$ denotes the contribution from the straight integration contour, which is given by eq. (2.19) with the v'-integration along the v'_r-axis with $v'_r > 0$. The residue's contribution $\Delta_P(\omega)$ is written as

$$\Delta_P(\omega) = -\pi \mathrm{i} \frac{(-\omega')^{1/2}}{a\sqrt{b}} \int_{-1}^{1} d\mu \; G[\omega, v' = (-\omega')^{1/2}, \mu]. \tag{2.21}$$

The condition $\omega' = 0$ gives $\omega = c^2/4b \equiv \omega_{br}$ which is called the branch frequency. In the limit of $\omega \to \omega_{br}$, we obtain from eqs. (2.19)–(2.21)

$$P_0(\omega) \to P(\omega_{br}) = \frac{1}{a\sqrt{b}} \int_{-1}^{1} d\mu \int_{0}^{\infty} dv' G(\omega, v', \mu) \tag{2.22}$$

$$\Delta_P(\omega) \simeq -\pi \mathrm{i} \frac{(\omega_{br} - \omega)^{1/2}}{a\sqrt{b}} \int_{-1}^{1} d\mu \; G[\omega, v' = 0, \mu]. \tag{2.23}$$

2.3.3 Normal modes and a continuum mode

For analytic continuation of $\phi(\omega)$ given by eq. (2.12), we need to take account of the poles defined by $D(\omega) = 0$ and the branch cut growing from the branch frequency ω_{br}. Comparing eqs. (2.13) and (2.14) with eq. (2.16), we obtain $2a = b = -\hat{\omega}_D/v_{Ti}^2$ and $c = k_{\|}$ where $\hat{\omega}_D \equiv 2\epsilon_n \omega_{*i} < 0$ is assumed. Then, the branch frequency is written as $\omega_{br} = c^2/4b = -k_{\|}^2 v_{Ti}^2/(4\hat{\omega}_D)$. For evaluating the inverse Laplace transform eq. (2.12), we take the integration contour L as shown in Fig. 2.2.

For $t > 0$, $\phi(t)$ is written as the sum of the contributions from the poles (normal modes) and the branch cut:

$$\phi(t) = \phi_p(t) + \phi_{br}(t) \tag{2.24}$$

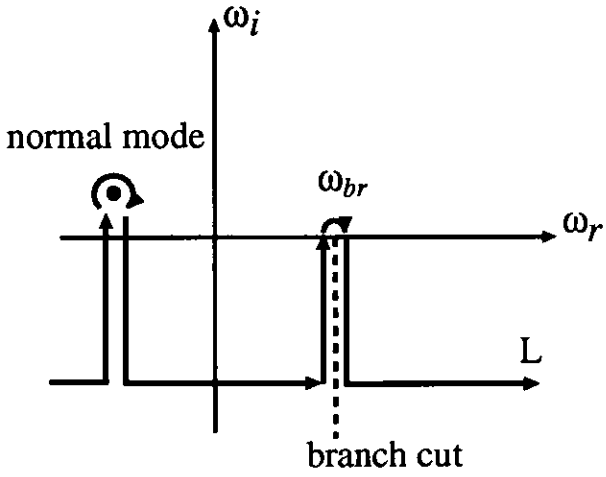

Figure 2.2: The integration contour L on the complex ω-plane for evaluating the inverse Laplace transform eq. (2.12). Dominant contributions to the integral are made by poles and a branch cut.

where the poles' (or normal modes') contribution is given by

$$\frac{e\phi_p(t)}{T_i} = -\mathrm{i}\sum_n \frac{I(\omega_n)}{\frac{dD}{d\omega}(\omega_n)}\mathrm{e}^{-\mathrm{i}\omega_n t} \tag{2.25}$$

and the contribution from the branch cut is written as

$$\begin{aligned}\frac{e\phi_{br}(t)}{T_i} &= \int_{C_{br}} \frac{d\omega}{2\pi}\mathrm{e}^{-\mathrm{i}\omega t}\left(\frac{I_0+\Delta_I}{D_0+\Delta_D}-\frac{I_0}{D_0}\right) \\ &= \mathrm{i}\mathrm{e}^{-\mathrm{i}\omega_{br}t}\int_{-\infty}^{0}\frac{d\omega_i}{2\pi}\mathrm{e}^{\omega_i t}\left[\frac{D_0\Delta_I - I_0\Delta_D}{D_0(D_0+\Delta_D)}\right]_{\omega=\omega_{br}+\mathrm{i}\omega_i}.\end{aligned} \tag{2.26}$$

The normal-mode frequencies ω_n in eq. (2.25) are determined by $D(\omega_n)=0$. In eq. (2.26), the branch cut C_{br} is taken as the straight line path from $\omega_{br}-\mathrm{i}\infty$ to $\omega_{br}-\mathrm{i}0$ and the functions $D_0(\omega)$, $I_0(\omega)$, $\Delta_D(\omega)$, and $\Delta_I(\omega)$ are defined in the same way as $P_0(\omega)$ and $\Delta_P(\omega)$ in eqs. (2.20) and (2.21). Thus $\Delta_D(\omega)$ and $\Delta_I(\omega)$ represent contributions from the resonant pole in the velocity space shown by Fig. 2.1 (b) and are written as

$$\Delta_I = 4\pi^2\frac{(\omega_{br}-\omega)^{1/2}}{(-\hat{\omega}_D)^{3/2}}\int_{-1}^{1}d\mu\left[\frac{J_0}{n_0}\langle\,\delta f_i(t=0)\,\mathrm{e}^{\mathrm{i}\boldsymbol{k}_\perp\cdot\boldsymbol{\rho}}\,\rangle\right]_{v'=v_0'} \tag{2.27}$$

and

$$\Delta_D = 4\pi^2\mathrm{i}\frac{(\omega_{br}-\omega)^{1/2}}{(-\hat{\omega}_D)^{3/2}}\cdot\int_{-1}^{1}d\mu\left[(\omega-\omega_{*T})\,{J_0}^2F_M\right]_{v'=v_0'} \tag{2.28}$$

respectively, where $v_0' = (\omega_{br} - \omega)^{1/2}$ and we have transformed the velocity variables as in eqs. (2.17) and (2.18).

As shown in eqs. (2.22) and (2.23) in the limit of $\omega \to \omega_{br}$, we have $D_0(\omega) \to D(\omega_{br})$, $I_0(\omega) \to D(\omega_{br})$, $\Delta_D(\omega) \simeq C_D(\omega_{br} - \omega)^{1/2}$, and $\Delta_I(\omega) \simeq C_I(\omega_{br} - \omega)^{1/2}$ where C_D and C_I are constants. Then, from eq. (2.26), we obtain the asymptotic behavior of the branch cut contribution to the potential as

$$\frac{e\phi_{br}(t)}{T_i} \simeq t^{-3/2} \mathrm{e}^{-\mathrm{i}\omega_{br}t} \frac{\mathrm{e}^{\mathrm{i}3\pi/4}}{4\sqrt{\pi}} \left[\frac{C_I}{D(\omega_{br})} - \frac{C_D\, I(\omega_{br})}{\{D(\omega_{br})\}^2} \right] \tag{2.29}$$

for $t \gg -1/\hat{\omega}_D$, where

$$\begin{aligned} C_I &= \frac{8\pi^2}{(-\hat{\omega}_D)^{3/2}} \frac{v_{Ti}^3}{n_0}\, \delta f_i \left(t = 0, v_\perp = 0, v_\parallel = -\frac{k_\parallel v_{Ti}^2}{2\hat{\omega}_D} \right), \\ C_D &= \frac{8\pi^{1/2}\mathrm{i}}{(-\hat{\omega}_D)^{3/2}} \left[\omega_{br} - \omega_{*i} \left\{ 1 + \eta_i \left(\frac{k_\parallel^2 v_{Ti}^2}{4\hat{\omega}_D^2} - \frac{3}{2} \right) \right\} \right] \\ &\quad \cdot \exp\left(-\frac{k_\parallel^2 v_{Ti}^2}{4\hat{\omega}_D^2} \right). \end{aligned} \tag{2.30}$$

Noting that $\delta n_i = \delta n_e = n_0 e\phi/T_e$ and comparing eq. (2.29) with eq. (2.9), we see that, for the initial value problem of the toroidal ITG mode, the potential and density perturbations derived from the branch cut integration show the same form of asymptotic behavior $\propto t^{-3/2}\mathrm{e}^{-\mathrm{i}\omega_{br}t}$ as the the density perturbation for the ballistic mode without interaction with the potential. [If we put $D_0(\omega) = 1$ with $\Delta_D = 0$ in eq. (2.26), the ballistic mode case in eq. (2.6) is reproduced.]

Now we find from eqs. (2.24), (2.25), and (2.29) that the long-time asymptotic behavior of the potential and density perturbations for the toroidal ITG mode is determined by the normal mode with the largest positive growth rate for the unstable case while it is dominated by the continuum mode for the stable case in which all normal modes decay faster than the continuum mode.

It should be remarked here that there is some arbitrariness about how to make a branch cut from the branch frequency. Different branch cuts make differences in definitions of $\phi_p(t)$ and $\phi_{br}(t)$ because of changes in complex-frequency regions where analytic continuation of

$D(\omega)$ and $I(\omega)$ is defined. However, it is obvious that the total perturbation $\phi(t) = \phi_p(t) + \phi_{br}(t)$ and its asymptotic behavior given by eq. (2.29) for the stable case should be independent of the way to make a branch.

2.4 Numerical examples

2.4.1 Dispersion relation

Following the prescription given in the previous section, we can calculate the dispersion function $D(\omega)$ analytically continued on the whole complex ω-plane. Here the dispersion relation $D(\omega) = 0$ is numerically solved to obtain the eigenfrequency $\omega_n = \omega_r + \mathrm{i}\gamma$ of the normal mode. Figure 2.3 shows the resultant normalized growth rate $L_n\gamma/v_{Ti}$ and real frequency $L_n\omega_r/v_{Ti}$ of the toroidal ITG mode as a function of the normalized poloidal wavenumber $k_\theta\rho_{Ti}$ for $\tau_e = 1$, $\epsilon_n = 0.25$, $\eta_i = 2.5$, and $k_\parallel R = 1/3,\ 1/2,\ 1$. We can see that, owing to the proper analytic continuation, the growth rate and real frequency are smoothly continued into the stable regions where the growth rate is negative. The stable regions are found for both small and large poloidal wavenumbers. Also, the growth rate decreases with the parallel wavenumber increased. For all curves shown in Fig. 2.3, the real frequency is smaller than the branch frequency so that the toroidal resonance is essential to the dispersion relation. The growth rate and real frequency for the nonresonant mode are not shown in Fig. 2.3.

Figure 2.4 shows the normalized growth rate $L_n\gamma/v_{Ti}$ (top) and real frequency $L_n\omega_r/v_{Ti}$ (bottom) of the toroidal ITG mode as a function of η_i for $\tau_e = 1$, $k_\theta\rho_{Ti} = 0.75$, $k_\parallel R = 1/2$, and $\epsilon_n = 0.1,\ 0.25,\ 0.4$. We can see that the growth rate increases with increasing η_i and that the real frequency has the negative sign corresponding to the ion diamagnetic rotation for larger values of η_i. Since we are able to calculate negative growth rates, we can clearly identify the critical η_i value which is shown in Fig. 2.4 to increase with increasing ϵ_n.

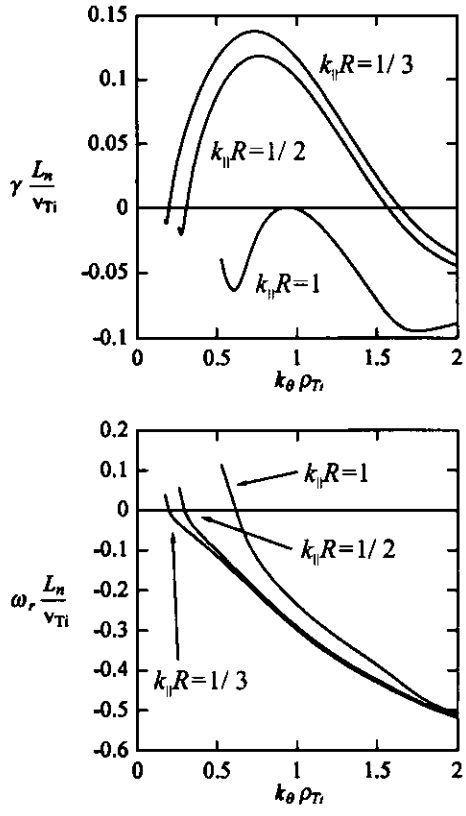

Figure 2.3: The normalized growth rate $L_n\gamma/v_{Ti}$ (top) and real frequency $L_n\omega_r/v_{Ti}$ (bottom) of the toroidal ITG mode as a function of the normalized poloidal wavenumber $k_\theta\rho_{Ti}$ for $\tau_e = 1$, $\epsilon_n = 0.25$, $\eta_i = 2.5$, and $k_{||}R = 1/3,\ 1/2,\ 1$.

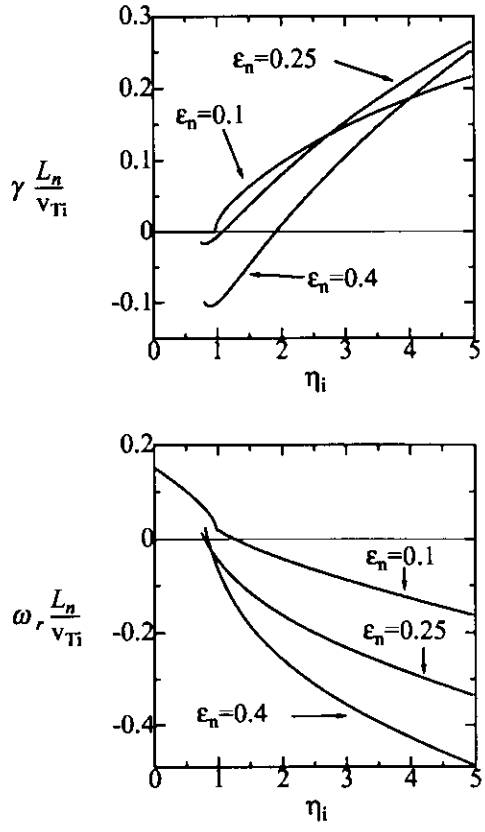

Figure 2.4: The normalized growth rate $L_n\gamma/v_{Ti}$ (top) and real frequency $L_n\omega_r/v_{Ti}$ (bottom) of the toroidal ITG mode as a function of η_i for $\tau_e = 1$, $k_\theta\rho_{Ti} = 0.75$, $k_\parallel R = 1/2$, and $\epsilon_n = 0.1$, 0.25, 0.4.

2.4.2 Solution of the initial value problem

Here let us consider an example of the initial value problem in which the initial perturbation is proportional to Maxwellian. Then, we use the same initial condition for the nonadiabatic distribution as in eq. (2.7) to obtain a compact expression for the gyrophase-averaged initial distribution function in eq. (2.13) as

$$\langle\, \delta f_i(t=0)\, \mathrm{e}^{-\mathrm{i}\boldsymbol{k}_\perp\cdot\boldsymbol{\rho}} \,\rangle = C_f\, J_0(k_\perp\rho)\, F_M\, \delta n(t=0) \tag{2.31}$$

with

$$C_f = -\tau_e + (1+\tau_e)/\Gamma_0(b_i) \tag{2.32}$$

where eqs. (2.1), (2.10) and (2.11) are used. We have $C_f \to 1$ in the small gyroradius limit $k_\perp\rho_{Ti} \to +0$. The density and potential perturbation at $t > 0$ are given by using eqs. (2.13), (2.14), (2.24)–(2.28), and the initial condition eq. (2.31).

Figure 2.5 shows time evolution of the toroidal ITG mode for the stable case where $\tau_e = 1$, $\epsilon_n = 0.25$, $\eta_i = 2.5$, $k_\parallel R = 0.5$, and $k_\theta\rho_{Ti} = 0.28$. In this case, the eigenfrequency of the normal mode and the branch frequency are given by $L_n\omega_n/v_{Ti} = 0.024 - 0.019\mathrm{i}$ and $L_n\omega_{br}/v_{Ti} = 0.056$. The potential amplitudes of the normal mode $\phi_p(t)$ (a solid curve) and the continuum mode $\phi_{br}(t)$ (a dotted curve) are shown in Fig. 2.5 (a). The total potential $\phi(t) = \phi_p(t) + \phi_{br}(t)$ is shown in Fig. 2.5 (b). The asymptotic behavior is well described by the analytical result given by eq. (2.29) which is shown by the dashed line in Fig. 2.5 (b). The cosine of the phase of the potential $\phi(t)$ is given in Fig. 2.5 (c) which clearly shows the change from the normal mode frequency to the branch frequency. Note that Figs. 2.5 (a)–(c) also show the behavior of the density perturbation because $\delta n_e = \delta n_i = n_0 e\phi/T_e$.

We find from these figures that, for the stable case, the temporal behavior of the ITG mode is described by the exponential dependence of the normal mode only near the initial time although the long-time asymptotic behavior is dominantly determined by the power-law decay of the continuum mode.

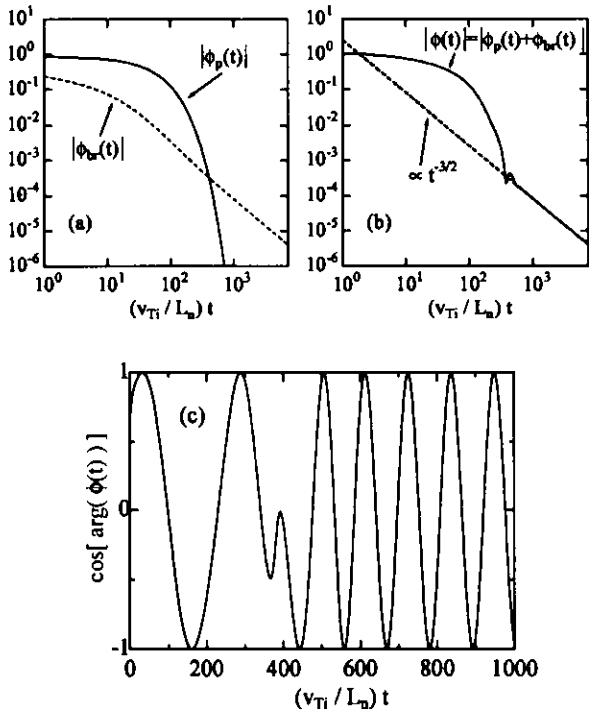

Figure 2.5: Time evolution of the toroidal ITG mode for the stable case where $\tau_e = 1$, $\epsilon_n = 0.25$, $\eta_i = 2.5$, $k_{||}R = 0.5$, and $k_\theta \rho_{Ti} = 0.28$. (a) The potential amplitudes of the normal mode $\phi_p(t)$ (a solid curve) and the continuum mode $\phi_{br}(t)$ (a dotted curve). (b) The total potential $\phi(t) = \phi_p(t) + \phi_{br}(t)$ normalized by the initial value $\phi(t = 0)$. (c) The cosine of the phase of the potential $\phi(t)$. Here the eigenfrequency of the normal mode and the branch frequency are given by $L_n\omega_n/v_{Ti} = 0.024 - 0.019\,\mathrm{i}$ and $L_n\omega_{br}/v_{Ti} = 0.056$. The dashed line in (b) represents the analytical result given by eq. (2.29) for the asymptotic limit.

Generally, the number of the normal modes for given parameters is more than one. Figures 2.3 and 2.4 show the growth rate and real frequency for the most unstable (or the least stable) normal mode. For the parameters used in Fig. 2.5, there exist an infinite number of stable normal modes with eigenfrequencies $L_n\omega_n/v_{Ti} = 0.024 - 0.019\mathrm{i}$, $-0.073 - 0.103\mathrm{i}$, $-0.463 - 0.565\mathrm{i}$, $\cdots$. However only the least stable normal mode is used in Fig. 2.5 since the results in Fig. 2.5 change little even if other rapidly decaying normal modes are added. Although the numerical time range may seem to be too long for collisionless assumption to be valid, it is much shorter than ion collision time ($10^3 L_n/v_{Ti} \sim 10^{-3}$ sec $\ll \tau_{ii} \sim 10^{-2}$sec) for typical reactor parameters with $T \sim 10$ keV, $n \sim 10^{20}\mathrm{m}^{-3}$, $L_n \sim 1\mathrm{m}$.

2.5 Conclusions

In this chapter, temporal evolution of the toroidal ITG mode has been studied by solving the initial value problem of the ion gyrokinetic equation combined with the electron Boltzmann relation and the charge neutrality condition.

For the toroidal ITG mode, temporal dependence of the density and potential perturbations is described by two types of behavior. One is well-known normal modes which change exponentially in time. Their frequencies and growth rates are determined by the dispersion relation and correspond to the poles of the Laplace-transformed potential function on the complex frequency plane. The other type is a continuum mode which is given by the integration of the Laplace-transformed potential function along a branch cut. Occurrence of the branch cut is due to the quadratic velocity dependence of the toroidal ∇B-curvature drift. The long-time asymptotic behavior of the continuum mode is characterized by oscillation at the branch frequency and power law decay $\propto t^{-3/2}$. This behavior is the same as that of the ballistic response obtained by the propagator of the gyrokinetic equation without taking account of interaction with the potential.

If the normal mode analysis shows the system to be unstable, the long-time behavior

is dominantly described by the normal mode with the largest growth rate. On the other hand, when the system is stable, only the normal modes are not enough for describing the temporal evolution of the toroidal ITG mode. In the stable case, the system is eventually dominated by the continuum mode since all the normal modes decay more rapidly.

In the future, we consider the fields associated with the test gyrokinetic particle. The noise associated with an ensemble of statistical independent dressed test gyrokinetic particles may be of importance for computer simulations of ITG turbulence.

Chapter 3

ITG Modes in Straight Helical Systems

3.1 Introduction

For toroidal systems such as tokamaks and stellarators, the properties of the ITG modes are significantly affected by the magnetic field geometry through the ∇B and curvature drift motion of particles. For tokamaks, the magnetic field strength is given by the large-aspect-ratio approximation as $B/B_0 = 1 - \epsilon_t \cos\theta$ where θ is the poloidal angle and $\epsilon_t = r/R$ is the inverse aspect ratio representing the toroidicity where r and R denote the minor and major radii, respectively. Many studies have been done on the ITG modes in tokamaks [8, 16, 17, 18, 19, 20, 21, 22, 23, 24, 25]. In this case, the ITG modes are confined mostly in the outside of the torus, $-\pi/2 < \theta < \pi/2$, which corresponds to the bad curvature region.

For helical systems, the magnetic field strength is approximately given by

$$B/B_0 = 1 - \epsilon_t \cos\theta - \epsilon_h \cos(L\theta - M\zeta), \tag{3.1}$$

where ζ is the toroidal angle and the term with $\epsilon_h \propto r^L$ in the right-hand side represents the helical ripple with the poloidal and toroidal polarity numbers denoted by L and M,

respectively. For example, we have $L = 2$ and $M = 10$ for LHD [13] and $L = 2$ and $M = 8$ for Compact Helical System (CHS) [31]. Since the helical magnetic ripple affects the particles' drift motion, the properties of the ITG modes stability in helical systems can be different from those in tokamaks [32].

In this chapter, we investigate the properties of the ITG modes for the helical systems with $L = 2$ and $2 \leq M \leq 10$ which are compared to the tokamak case. Especially, the effects of the toroidal polarity number M on the dispersion relation and the mode structure of the ITG modes are studied. This work is published in [33].

3.2 Kinetic ITG Mode Equation for Helical Systems

Here we consider a high-temperature collisionless plasma and assume that, in the presence of the electrostatic perturbation ϕ, the perturbed electron density is described by the adiabatic (or Boltzmann) response $\delta n_e = (e\phi/T_e)n_0$. The perturbed ion distribution function is written as $\delta f_i = -(e\phi/T_i)n_0 F_M + h \exp(-\mathrm{i}\, \boldsymbol{k}_\perp \cdot \boldsymbol{\rho})$ where $F_M \equiv \pi^{-3/2} v_{Ti}^{-3} \exp(-v^2/v_{Ti}^2)$ is the Maxwellian distribution function, $v_{Ti} \equiv (2T_i/m_i)^{1/2}$ is the thermal velocity for the ions with the mass m_i and the temperature T_i, $\boldsymbol{\rho} \equiv \boldsymbol{b} \times \boldsymbol{v}/\Omega_i$ ($\boldsymbol{b} = \boldsymbol{B}/B$) is the ion gyroradius vector, and $\Omega_i \equiv eB/(m_i c)$ is the ion gyrofrequency. The non-adiabatic part of the distribution function h is determined by the linear gyrokinetic equation

$$\left(\omega - \omega_D + \mathrm{i} v_\parallel \boldsymbol{b} \cdot \nabla\right) h = (\omega - \omega_{*T}) \frac{e\phi}{T_i} J_0(k_\perp \rho) n_0 F_M. \tag{3.2}$$

Here ω is the frequency of the perturbation, $\omega_D = \boldsymbol{k}_\perp \cdot \boldsymbol{v}_D$ is the ion ∇B-curvature drift frequency, J_0 is the Bessel function of order zero, and $\omega_{*T} = \omega_{*i}[1 + \eta_i\{(v/v_{Ti})^2 - 3/2\}]$ where $\eta_i \equiv d\ln T_i/d\ln n_0$ is the ratio of the ion temperature gradient to the density gradient, $\omega_{*i} \equiv -\tau_e^{-1}\omega_{*e}$ is the ion diamagnetic drift frequency, $\tau_e \equiv T_e/T_i$ is the ratio between the electron and ion temperatures, $\omega_{*e} \equiv ck_\theta T_e/(eBL_n)$ is the electron diamagnetic drift frequency, $L_n = -(d\ln n_0/dr)^{-1}$ is the density gradient scale length, and k_θ is the poloidal wavenumber.

We use the ballooning representation [34, 35] and write the perpendicular wavenumber vector as $\boldsymbol{k}_\perp = k_\alpha(\nabla\alpha + \theta_k\nabla q)$ where q is the safety factor, $\alpha = \zeta - q\theta$ is the label for magnetic field line, and $k_\alpha = -n$ represents the toroidal mode number, which is related to the poloidal wavenumber as $k_\theta = nq/r$. In the present work, we assume that $\theta_k = 0$. We consider a large aspect-ratio and low β toroidal system and use Eq. (3.1) to give the ion ∇B-curvature drift frequency as

$$\begin{aligned}\omega_D &= 2(L_n/r)\omega_{*i}(v_\parallel^2 + v_\perp^2/2)/v_{Ti}^2\ [\epsilon_t\{\cos\theta + \hat{s}\theta\sin\theta\} \\ &\quad + L\epsilon_h\{\cos(L\theta - M\zeta) + \hat{s}\theta\sin(L\theta - M\zeta)\}] \end{aligned} \tag{3.3}$$

where $\hat{s} = (r/q)dq/dr$ is the shear parameter.

Neglecting the trapped ions, integrating the gyrokinetic equation (3.2) along the field line with the boundary conditions $h(\theta \to \pm\infty) = 0$, and substituting it into the charge neutrality condition $e\phi/T_e = \delta n_e/n_0 = \delta n_i/n_0 = -e\phi/T_i + \int d^3v J_0(k_\perp\rho)h$, we obtain the integral equation which is written as

$$\left(1 + \frac{T_e}{T_i}\right)\phi(k) = \int_{-\infty}^{+\infty}\frac{dk'}{\sqrt{2\pi}}K(k,k')\phi(k') \tag{3.4}$$

with

$$\begin{aligned}K(k,k') &= -\,\mathrm{i}\int_{-\infty}^{0}\omega_{*e}d\tau\frac{\sqrt{2}\mathrm{e}^{-\mathrm{i}\omega\tau}}{\sqrt{a}(1+a)\sqrt{\lambda}}\mathrm{e}^{-(k-k')^2/4\lambda} \\ &\times\left[\frac{\omega}{\omega_{*e}}\tau_e + 1 - \frac{3}{2}\eta_i + \frac{\eta_i(k-k')^2}{4a\lambda} + \frac{2\eta_i}{(1+a)}\left(1 - \frac{k_\perp^2 + k_\perp'^2}{2(1+a)\tau_e}\right.\right. \\ &\left.\left. + \frac{k_\perp k_\perp'}{(1+a)\tau_e}\frac{I_1}{I_0}\right)\right]\Gamma_0(k_\perp, k_\perp') \end{aligned} \tag{3.5}$$

where $I_j = I_j(k_\perp k_\perp'/[(1+a)\tau_e])$ $(j = 0, 1)$ are the modified Bessel functions of j-th order, $\lambda = (\omega_{*e}\tau)^2(\hat{s}\epsilon_n/q)^2/\tau_e a$, $\theta = k/\hat{s}k_\theta$, $\theta' = k'/\hat{s}k_\theta$, $\Gamma_0(k_\perp, k_\perp') = I_0(k_\perp k_\perp'/[(1+a)\tau_e])$, $k_\perp^2 = k_\theta^2 + k^2$, $k_\perp'^2 = k_\theta^2 + k'^2$, and

$$\begin{aligned}a &= 1 - \mathrm{i}\ 2(L_n/r)\tau_e^{-1}\omega_{*e}\tau/(\theta - \theta') \\ &\quad\times(\epsilon_t\left[(\hat{s}+1)(\sin\theta - \sin\theta') - \hat{s}(\theta\cos\theta - \theta'\cos\theta')\right]\end{aligned}$$

$$
\begin{aligned}
&+ (L\epsilon_h/(L - Mq))\,[\{\hat{s}/(L - Mq) + 1\} \\
&\times \{\sin((L - Mq)\theta - M\alpha) - \sin((L - Mq)\theta' - M\alpha))\} \\
&- \hat{s}\,\{\theta\cos((L - Mq)\theta - M\alpha) - \theta'\cos((L - Mq)\theta' - M\alpha))\}])\,.
\end{aligned}
\tag{3.6}
$$

Here the wavenumber variables k_θ, k, and k' are normalized by ρ_s^{-1} ($\rho_s = \sqrt{2T_e/m_i}/\Omega_i$) and $\epsilon_h \propto r^L$ is used. The integral equation (3.4) with the boundary conditions $\phi(\theta \to \pm\infty) = 0$ determines the complex-valued eigenfrequency and eigenfunction of the ITG mode for the helical system. If we put $\epsilon_h = 0$, the integral ITG mode equation (3.4) with Eqs. (3.5) and (3.6) reduces to the one given by Dong, *et al.* for the tokamak case [16].

3.3 Numerical Results

Here we numerically solve the integral equation (3.4) with the boundary conditions $\phi(\theta \to \pm\infty) = 0$ to obtain the growth rate, the real frequency, and the eigenfunction of the ITG mode for the $L = 2$ helical systems with various M numbers. Since we are concerned with the effects of the helical ripple, we neglect the toroidicity by putting $\epsilon_t = 0$ (straight helical system) for simplicity. Typical parameters used here are $q = 2$, $k_\theta\rho_{Ti} = 0.75$, $T_i/T_e = 1$, $L_n/R_0 = 0.2$, $L_n\epsilon_h/r = 0.2$, and $\hat{s} = -1$ (negative shear). We also treat a single field line labelled by $\alpha = 0$.

Figure 3.1 shows the normalized real frequency ω_r/ω_{e*} and growth rate ω_i/ω_{e*} of the ITG mode as a function of M for $\eta_i = 3, 4, 6, 8$. Other parameters used here are the same as mentioned above. The real frequencies obtained here are all negative, which corresponds to the ion diamagnetic rotation. The growth rate decreases with increasing M.

Corresponding to the cases for $M = 2, 3, 4, 5, 8, 10$ in Fig. 3.2, the profiles of the eigenfunction ϕ and the helical drift frequency $\propto \cos[(L - Mq)\theta] + \hat{s}\theta\sin[(L - Mq)\theta]$ in the covering space (θ-space) are plotted in Fig. 3.2. The regions where the helical drift frequency is positive (negative) corresponds to bad (good) curvature. As M increases, the

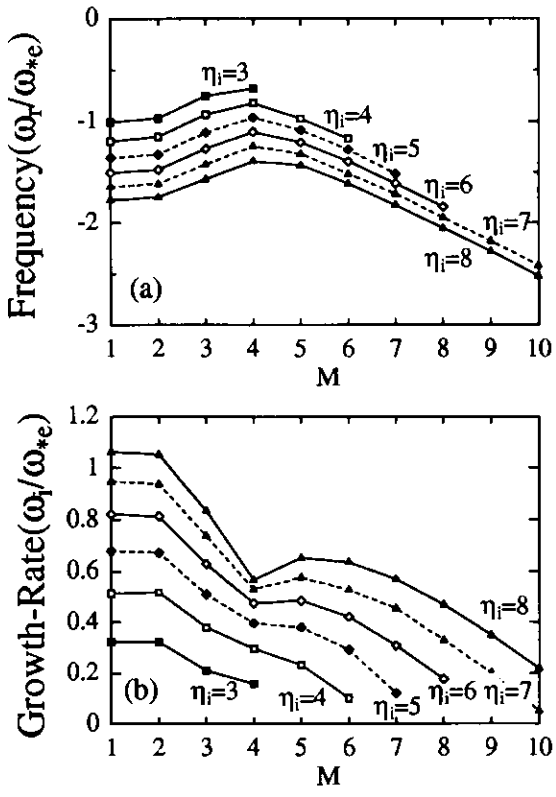

Figure 3.1: The normalized (a) real frequency ω_r/ω_{e*} and (b) growth rate ω_i/ω_{e*} of the ITG mode as a function of M for various η_i's. Here $q = 2$, $k_\theta \rho_{Ti} = 0.75$, $T_i/T_e = 1$, $L_n/R_0 = 0.2$, $L_n \epsilon_h / r = 0.2$, $\epsilon_t = 0$, and $\hat{s} = -1$.

eigenfunction ϕ becomes more rippled in the covering space and has a larger amplitude in the good curvature region, which is related to the reduction of the growth rate for larger M.

In the cases with large M like $M = 8$ (CHS) and $M = 10$ (LHD), a positive growth rate for the ITG mode cannot be found for $\eta_i < 4$, with the other parameters as given above. Unstable ITG modes are found for $M = 8$ and 10 with the very large temperature gradient (or very small density gradient) $\eta_i = 6, 8$ and they have more negative frequencies and more rippled eigenfunctions as shown in Figs. 3.1 and 3.2.

3.4 Conclusions

In this chapter, the ITG mode equation was numerically solved for a straight helical system with the poloidal period number $L = 2$, and the effects of the toroidal period number M on the dispersion relation and the mode structure of the ITG mode were studied. Field ripple with larger M reduces the growth rate of the ITG mode. This stabilizing effect is understood based on the structure of the eigenfunction along the field line as follows. As M increases, the connection length between the good and bad curvature regions becomes shorter and the eigenfunction enters the good curvature region, which leads to the stabilization. The stabilization by the short connection length is consistent with local kinetic limit. Then, significantly large temperature gradients are necessary to destabilize the ITG modes in straight helical systems with large $M(\simeq 10)$.

The next chapter shows how the ITG mode characters are changed by the combination of toroidicity and helical ripples.

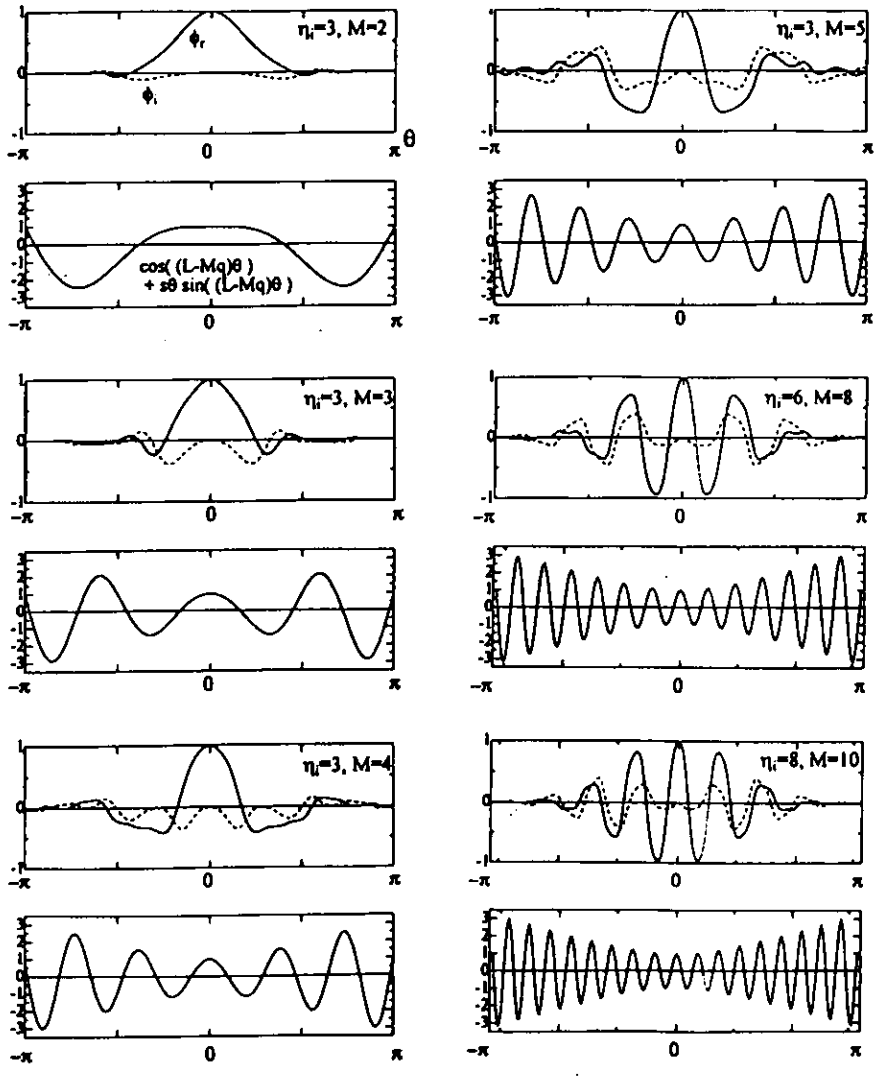

Figure 3.2: The profiles of the eigenfunction ϕ and the helical drift frequency $\propto \cos[(L - Mq)\theta] + \hat{s}\theta \sin[(L - Mq)\theta]$ in the covering space (θ-space) for $M = 2, 3, 4, 5, 8, 10$. Other parameters are the same as in Fig. 3.1.

Chapter 4

ITG Modes in Toroidal Helical Systems

4.1 Introduction

In helical systems such as LHD, the drift motions are driven not only by the toroidicity but also by the helicity (helical ripples). The magnetic field strength for the large aspect ratio helical system is given by (3.1). For tokamaks ($\epsilon_h = 0$), the ITG mode is localized like a Gaussian function in the outer region of the torus $-\pi/2 < \theta < \pi/2$, which is called the bad curvature region since the ion drift motions in this region destabilize the ITG mode. This local destabilization is brought by the toroidicity. For helical systems ($\epsilon_h \neq 0$), the equilibrium depends not only on θ but also on ζ, and the distribution of bad curvature regions becomes more complicated due to the helicity combined with the toroidicity. Another important feature of the helical systems is the negative magnetic shear in contrast with the positive magnetic shear of the conventional tokamaks. These characteristics are expected to bring about different effects on the ITG mode.

In this chapter, in order to take account of kinetic effects such as wave-particle interactions and finite ion gyroradius, we use the ion gyrokinetic equation [26, 27] to obtain

the dispersion relation and the mode structure of the linear electrostatic ITG mode in the LHD-like helical system, which is compared with the tokamak ITG mode. Recently, similar gyrokinetic analyses have been done on the ITG mode in the helias configuration [32] and in the quasi-axisymmetric stellarators [36]. Here, assuming the low β(= the ratio of the plasma pressure to the magnetic pressure) large aspect ratio toroidal plasma with a circular cross section of the flux surface, we clarify the effects of the ion ∇B-curvature drift motion in the helical system with the model magnetic field given by eq. (3.1).

The rest of this chapter is organized as follows. In § 4.2, the dispersion relation of the linear ITG mode in the helical system is derived as a kinetic integral equation from the ion gyrokinetic equation, the adiabatic electron assumption, and the quasineutrality condition. In § 4.3, results from numerical solutions of the integral equation are presented to show dependences of the ITG mode properties on various plasma equilibrium parameters such as the helical ripple intensity, safety factor, magnetic shear, ballooning angle, poloidal wavenumber, temperature and density gradients. In § 4.4, conclusions are given. These works are to be published in [37].

4.2 Dispersion Relation

As seen in § 3.2, the kinetic integral equation to give the dispersion relation of the ITG mode in the helical system is derived from the electron adiabatic response $\delta n_e = e\phi/T_e$ and the collisionless linear gyrokinetic equation for ions (3.2), and the quasineutrality. In the present work, following Dong *et al.* [16] and Romanelli [21], effects of the magnetic configuration are taken into account only through the ion ∇B-curvature drift motion. Trapped particle effects are neglected here since mainly the passing ions drive the ITG modes. We consider a large aspect ratio and low β toroidal system, for which the magnetic field strength is given by eq. (3.1). Then, the ion ∇B-curvature drift frequency is given by

$$\omega_D \;=\; 2(L_n/r)\omega_{*i}(\, v_\parallel^2 + v_\perp^2/2 \,)/v_{Ti}^2$$

$$\times \Big[\epsilon_t \{\cos\theta + \hat{s}(\theta - \theta_k)\sin\theta\}$$
$$+ L\epsilon_h \{\cos(L\theta - M\zeta) + \hat{s}(\theta - \theta_k)\sin(L\theta - M\zeta)\} \Big], \tag{4.1}$$

which reduces to (3.3) for the case of $\theta_k = 0$. Here, the ballooning representation [34, 35] is used. The perpendicular wavenumber vector is written as $\boldsymbol{k}_\perp = k_\alpha(\nabla\alpha + \theta_k \nabla q)$, $q(r)$ is the safety factor, $\alpha = \zeta - q\theta$ is the label of the magnetic field line, and $k_\alpha = -n$ represents the toroidal mode number, which is related to the poloidal wavenumber as $k_\theta = nq/r$. Using the independent variables (q, α, θ) as the spatial coordinates, (3.2) becomes the ordinary differential equation with respect to θ.

Integrating the gyrokinetic equation (3.2) along the field line with the boundary conditions $h(\theta \to \pm\infty) = 0$, and substituting it into the quasineutrality condition $\delta n_i = -(e\phi/T_i)n_0 + \int d^3v J_0(k_\perp\rho)h = \delta n_e = (e\phi/T_e)n_0$, we obtain the integral equation,

$$\left(1 + \frac{T_e}{T_i}\right)\phi(\omega, k) = \int_{-\infty}^{+\infty} \frac{dk'}{\sqrt{2\pi}} K(k, k')\phi(\omega, k') \tag{4.2}$$

with

$$K(k, k') = -\mathrm{i}\int_{-\infty}^{0} \omega_{*e} d\tau \frac{\sqrt{2}\mathrm{e}^{-\mathrm{i}\omega\tau}}{\sqrt{a}(1+a)\sqrt{\lambda}} \mathrm{e}^{-(k-k')^2/4\lambda}$$
$$\times \left[\frac{\omega}{\omega_{*e}}\tau_e + 1 - \frac{3}{2}\eta_i + \frac{\eta_i(k-k')^2}{4a\lambda} + \frac{2\eta_i}{(1+a)}\right.$$
$$\left.\left(1 - \frac{k_\perp^2 + k_\perp'^2}{2(1+a)\tau_e} + \frac{k_\perp k_\perp'}{(1+a)\tau_e}\frac{I_1}{I_0}\right)\right] \Gamma_0(k_\perp, k_\perp'), \tag{4.3}$$

where $I_j = I_j(k_\perp, k_\perp'/(1+a)\tau_e))$ $(j = 0, 1)$ are the modified Bessel functions of j-th order, $\lambda = (\omega_{*e}\tau)^2(\hat{s}\epsilon_n/q)^2/\tau_e a$, $\epsilon_n = L_n/R$, $k = \hat{s}k_\theta(\theta - \theta_k)$, $k' = \hat{s}k_\theta(\theta' - \theta_k)$, $\Gamma_0(k_\perp, k_\perp') = I_0(\, k_\perp k_\perp'/[(1+a)\tau_e]\,)\exp[\,-(k_\perp^2 + k_\perp'^2)/2\tau_e(1+a)\,]$, $k_\perp^2 = k_\theta^2 + k^2$, $k_\perp'^2 = k_\theta^2 + k'^2$, and

$$a = 1 - \mathrm{i}2(L_n/r)\tau_e^{-1}\omega_{*e}\tau/(\theta - \theta')$$
$$\times \Big(\epsilon_t [\,(\hat{s}+1)(\sin\theta - \sin\theta') - \hat{s}\{(\theta - \theta_k)\cos\theta - (\theta' - \theta_k)\cos\theta'\}\,]$$
$$+ (L\epsilon_h(L - Mq)^{-1}) \Big[\left\{\hat{s}(L - Mq)^{-1} + 1\right\}$$
$$\times \{\sin(\,(L - Mq)\theta - M\alpha\,) - \sin(\,(L - Mq)\theta' - M\alpha\,)\}$$

$$- \hat{s} \Big\{ (\theta - \theta_k) \cos(\ (L - Mq)\theta - M\alpha\ ) \\ -(\theta' - \theta_k) \cos(\ (L - Mq)\theta' - M\alpha\ ) \Big\} \ \Big] \ \Big) . \tag{4.4}$$

Here, the wavenumber variables k_θ, k, and k' are normalized by ρ_s^{-1} ($\rho_s = \sqrt{2T_e/m_i}/\Omega_i$) and $\epsilon_h(r) \propto r^L$ is used.

The integral equation (4.2) with the boundary conditions $\phi(\theta \to \pm\infty) = 0$ determines the complex-valued eigenfrequency and eigenfunction of the ITG mode for the helical system. If we put $\epsilon_h = 0$, the integral ITG mode equation (4.2) with eqs. (4.3) and (4.4) reduces to the one given by Dong, *et al.* for the tokamak case [16]. Compared to the tokamak case, the dispersion relation for the helical system depends on additional parameters ϵ_h/ϵ_t, L, M, and α, Then, the eigenfrequency is written as

$$\omega = \omega(q, \hat{s}, \theta_k, \alpha, k_\theta, \eta_i, \epsilon_n, \tau_e, \epsilon_h/\epsilon_t, L, M). \tag{4.5}$$

In the next section, eq. (4.2) is numerically solved to investigate dependences of the ITG mode real frequency, growth rate, and structure on these parameters. Our numerical code can calculate both positive and negative growth rates with proper analytic continuation of the dispersion relation in the complex frequency plane [29, 30, 38]. Detailed procedures for the analytic continuation are shown in [38].

4.3 Numerical Results

In this section, we numerically solve the integral equation (4.2) with the boundary conditions $\phi(\theta \to \pm\infty) = 0$ to obtain the real frequency, growth rate, and eigenfunction of the ITG mode for the helical system with $L = 2$ and $M = 10$ (corresponding to the LHD case). As the standard parameters for the numerical calculation, we use $L = 2$, $M = 10$, $\epsilon_h/\epsilon_t = 1$, $q = 2$, $\hat{s} = -1$, $\tau_e = 1$, $\eta_i = 3$, $\epsilon_n = 0.3$, $\theta_k = 0$, $\alpha = 0$, and $k_\theta \rho_{Ti} = 0.65$. Here, $\rho_{Ti} = v_{Ti}/\Omega_i$ is the ion thermal gyroradius. These parameters are such that they

correspond to those at the magnetic surface $r/a = 0.6$ of the typical NBI-heated hydrogen plasma in LHD [15] with $B = 2.75T$, $T_i = T_e = 1.6keV$, $n = 0.7 \times 10^{19}m^{-3}$, $R = 3.6m$, $a = 0.6m$, $L_n = 1m$ and $L_{Ti} = 0.36m$. The field line $\alpha = 0$ passes through the point where magnetic field strength B has its smallest value on the magnetic flux surface. Also, $\theta_k = 0$ is the poloidal angle where the radial wavenumber k_r vanishes since $k_r = \hat{s}k_\theta(\theta - \theta_k)$. Therefore, the ITG mode is considered to become the most unstable for $\alpha = 0$ and $\theta_k = 0$. As seen later, the growth rate has a peak around the poloidal wavenumber $k_\theta \rho_{Ti} = 0.65$. Then, using the LHD parameters shown above, we obtain the electron diamagnetic frequency $\omega_{*e} = 1.8 \times 10^5 sec^{-1}$ and the poloidal wavelength $\lambda_\theta = 2\pi/k_\theta = 2.0 \times 10^{-2}m$ for $k_\theta \rho_{Ti} = 0.65$.

Here, we write the nondimensional factor, which represents the poloidal structure of the ∇B-curvature drift frequency, as

$$\begin{aligned} G(\theta) &= \cos\theta - \hat{s}(\theta - \theta_k)\sin\theta \\ &\quad -(\epsilon_h/\epsilon_t)L\Big[\cos\Big((L - Mq)\theta - M\alpha\Big) \\ &\quad -\hat{s}(\theta - \theta_k)\sin\Big((L - Mq)\theta - M\alpha\Big)\Big], \end{aligned} \tag{4.6}$$

which we call a curvature factor hereafter. It should be noted that, for $k_\theta > 0$, the sign of $G(\theta)$ is opposite to that of ω_D in eq. (4.1) because $L_n\omega_{*i} < 0$. For $G(\theta) > 0$, the poloidal ion ∇B-curvature drift motion is in the same direction as the ion diamagnetic rotation at the poloidal angle θ. Such poloidal region is called a bad curvature region because the destabilization of the modes occurs there. On the other hand, in the good curvature region ($G(\theta) < 0$), the ion magnetic drift is in the direction of the electron diamagnetic direction, and the modes are stabilized. For the helical system with $\epsilon_h/\epsilon_t \sim 1$ and $L \ll Mq$, the connection length between adjacent good and curvature regions is roughly given by Rq/M.

In the following subsections, we investigate dependences of the ITG mode properties on the equilibrium parameters in the regions around the standard parameters.

4.3.1 Helical ripple effects

Effects of the parameter ϵ_h/ϵ_t on the normalized real frequency ω_r/ω_{*e} [$\omega_r = \mathrm{Re}(\omega)$], the normalized growth rate γ/ω_{*e} [$\gamma = \mathrm{Im}(\omega)$], and the eigenfunction $\phi(\theta) = \phi_r + \mathrm{i}\phi_i$ are shown in Figs. 4.1 and 4.2. The parameters used here are the same as the standard ones (see the first paragraph of this section) except for ϵ_h/ϵ_t. The case of $\eta_i = 4$ is also plotted in Fig. 4.1. No helical ripple case $\epsilon_h/\epsilon_t = 0$ corresponds to the negative shear tokamak. With increasing ϵ_h/ϵ_t, the fine spatial structure of helical ripples appears and the connection length between adjacent good and bad curvature regions becomes shorter as seen from $G(\theta)$ in Fig. 4.2. The large helical ripples can produce the good curvature region even in the outside of the torus. Then, the eigenfunction enters not only the bad curvature region but also the good curvature region. That results in the monotonic decrease of the growth rate γ with increasing ϵ_h/ϵ_t. On the other hand, the real frequency is weakly dependent on ϵ_h/ϵ_t, and keeps the negative sign, which implies the wave propagation in the ion diamagnetic direction.

Using the ballooning transform [34],

$$\phi(r,\theta,\zeta) = \sum_{j=-\infty}^{+\infty} \phi(\theta + 2\pi j)\exp[-in\{\zeta - q(r)(\theta + 2\pi j - \theta_k)\}], \tag{4.7}$$

we obtain the three dimensional distribution of the electrostatic potential $\phi(r,\theta,\zeta)$ from the one dimensional eigenfunction $\phi(\theta)$. In eq. (4.7), the radial dependence of $\phi(r,\theta,\zeta)$ are considered only through $q(r) \simeq q(r_s) + (\hat{s}q/r)(r - r_s)$ where r_s denotes the radial position of a given magnetic surface. Thus, the three dimensional structure given by eq. (4.7) is valid only in the neighborhood of the magnetic surface $r = r_s$. The potential distribution $\phi(r,\theta,\zeta)$ in the region ($1.8 \le q \le 2.2$, $0 \le \zeta \le 2\pi/5$) around the $q = 2$ surface, which corresponds to Fig. 4.2 (b-1) (the case of the standard parameters), is shown in Fig. 4.3, where the toroidal mode number is determined from $k_\theta = nq/r = 0.65\rho_{Ti}^{-1}$ as $n = 56$. We can see the poloidal localization of the mode structure accompanied with its radial extension.

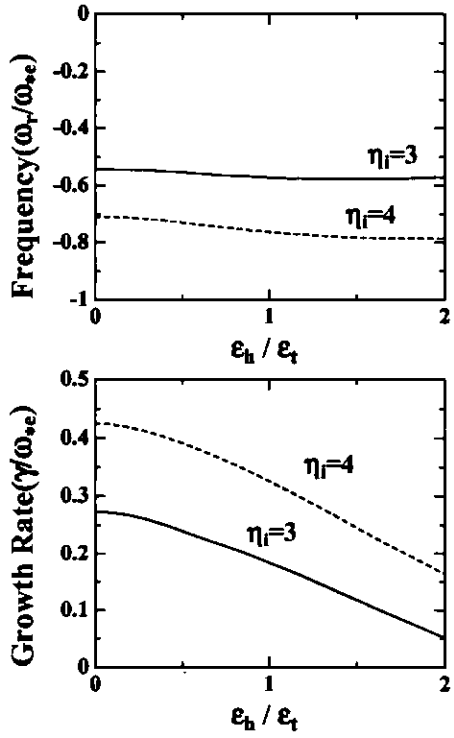

Figure 4.1: Normalized real frequency ω_r/ω_{*e} (top) and growth rate γ/ω_{*e} (bottom) as a function of ϵ_h/ϵ_t for $L = 2$, $M = 10$, $q = 2$, $\hat{s} = -1$, $\theta_k = 0$, $\alpha = 0$, $\eta_i = 3,\ 4$, $\epsilon_n = 0.3$, and $k_\theta \rho_{Ti} = 0.65$.

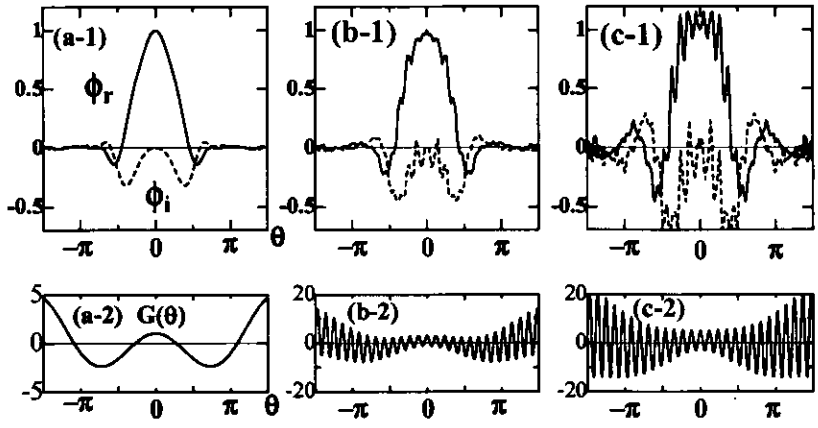

Figure 4.2: Eigenfunction $\phi(\theta) = \phi_r + i\phi_i$ and curvature factor $G(\theta)$ for $\epsilon_h/\epsilon_t = 0$ (a-1,2), $\epsilon_h/\epsilon_t = 1$ (b-1,2), and $\epsilon_h/\epsilon_t = 2$ (c-1,2). Here, $\theta = 0$ and $\theta = \pm\pi$ correspond to the outermost and innermost points on the toroidal magnetic surface, respectively. The other parameters are $L = 2$, $M = 10$, $q = 2$, $\hat{s} = -1$, $\theta_k = 0$, $\alpha = 0$, $\eta_i = 3$, $\epsilon_n = 0.3$, and $k_\theta \rho_{Ti} = 0.65$.

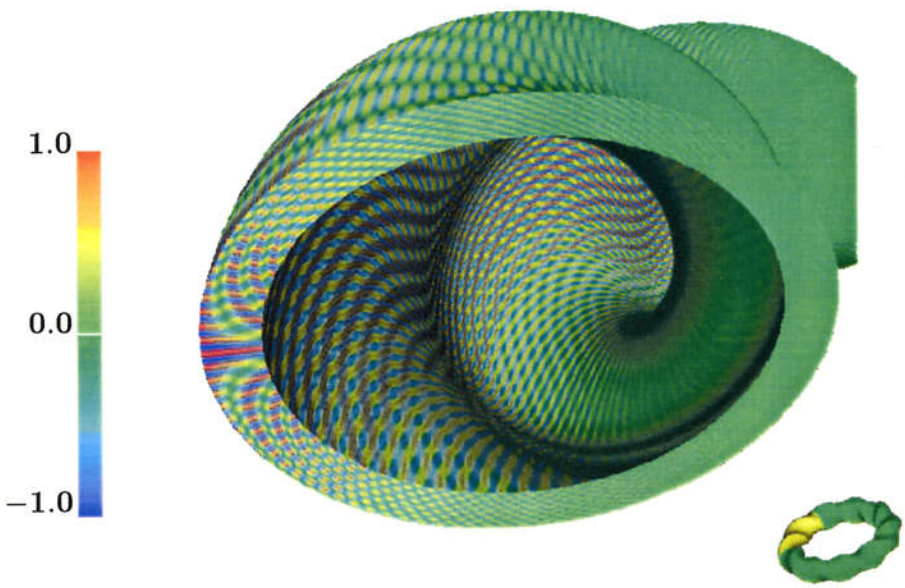

Figure 4.3: The three dimensional distribution of the real part of the potential function $\phi(r, \theta, \zeta)$ in the region $(1.8 \leq q \leq 2.2,$ $0 \leq \zeta \leq 2\pi/5)$ around the $q = 2$ surface. The potential values are shown by colors. The same parameters as in Fig. 2 (b-1) are used.

4.3.2 Effects of the safety factor q

Figure 4.4 shows the normalized real frequency and growth rate as a function of the safety factor q (the rotational transform is given by $\iota = q^{-1}$). The parameters used here are the same as the standard ones (see the first paragraph of this section) except for q. Also, the negative shear tokamak case with the same parameters except for $\epsilon_h/\epsilon_t = 0$ is plotted in Fig. 4.4. The growth rate for the helical case ($\epsilon_h/\epsilon_t = 1$) is smaller than for the tokamak case due to the stabilization effect of the helical ripples as explained in the previous subsection. We can see that the real frequency is weakly dependent on q although the growth rate becomes smaller for smaller q (larger ι) for both the tokamak and the helical cases. As seen in Fig. 4.2, for both cases, the width of the eigenfunction along the field line scales by the connection length Rq between the inside and outside of the torus. Therefore, the effective parallel wavelength $k_{||}^{-1} \sim Rq$ and the parallel phase velocity $\omega/k_{||}$ of the mode are reduced when q decreases. Then, the Landau damping becomes stronger, which is considered a stabilization mechanism for smaller q.

4.3.3 Effects of the magnetic shear $\hat{s}$

Figure 4.5 shows the normalized real frequency and growth rate as a function of the magnetic shear parameter $\hat{s}$. The parameters used here are the same as the standard ones (see the first paragraph of this section) except for $\hat{s}$. The negative shear tokamak case with the same parameters except for $\epsilon_h/\epsilon_t = 0$ is plotted in Fig. 4.5. It should be noted that the validity of the ballooning representation is lost in the limit $\hat{s} \to 0$ although the real frequency and growth rate for $\hat{s} = 0$ are plotted in Fig. 4.5. We see that, for both tokamak and helical cases, the growth rate has a peak at $\hat{s}_p \simeq 0.5$ in the positive shear region. As $|\hat{s} - \hat{s}_p|$ increases, the growth rate monotonically decreases, and the growth rate for negative shear $\hat{s} < 0$ is smaller than for positive shear $\hat{s} > 0$ with the same $|\hat{s}|$. The same tendency has been observed in the works on negative shear tokamaks [18, 39]. The real frequency

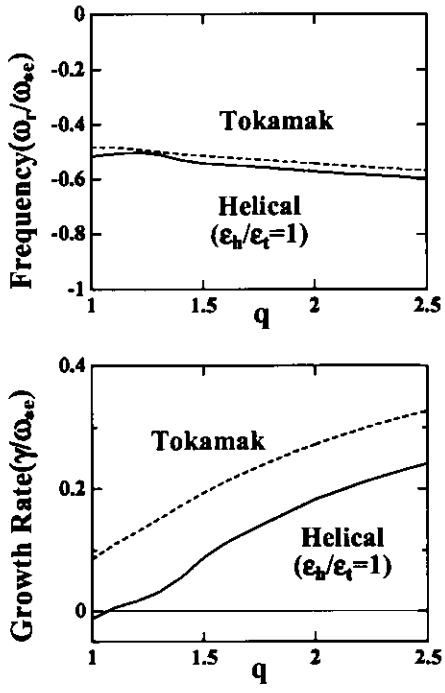

Figure 4.4: Normalized real frequency ω_r/ω_{*e} (top) and growth rate γ/ω_{*e} (bottom) as a function of the safety factor q for $L = 2$, $M = 10$, $\hat{s} = -1$, $\epsilon_h/\epsilon_t = 1$, $\theta_k = 0$, $\alpha = 0$, $\eta_i = 3$, $\epsilon_n = 0.3$, and $k_\theta \rho_{Ti} = 0.65$. The negative shear tokamak case with the same parameters except for $\epsilon_h/\epsilon_t = 0$ is plotted by the dotted line.

for $\hat{s} > 0$ takes more negative values than for $\hat{s} < 0$. Figure 4.6 shows the eigenfunction $\phi(\theta) = \phi_r + i\phi_i$ and the curvature factor $G(\theta)$ for both tokamak and helical cases with $\hat{s} = 1, 0.5, -1$. It is understood from Fig. 4.6 that the reduction of the growth rate for the negative shear case is due to the reduction of the bad curvature region in the torus outside.

4.3.4 Effects of the ballooning angle θ_k

Since $k_r = \hat{s}k_\theta(\theta - \theta_k)$, θ_k represents the poloidal angle, at which the radial wavenumber k_r vanishes and accordingly the finite gyroradius stabilization effect is weakest. Thus, the mode tends to be poloidally localized around $\theta = \theta_k$. Also, when we consider a rotating plasma, it is important to take account of θ_k-dependence [6, 40, 41, 42]. Figure 4.7 shows the normalized real frequency and growth rate as a function of θ_k. The parameters used here are the same as the standard ones (see the first paragraph of this section) except for θ_k. The negative shear tokamak case with $\epsilon_h/\epsilon_t = 0$ is also plotted in Fig. 4.7. It is seen in Fig. 4.7 that the real frequency is a slightly decreasing function of θ_k, which is a contrast to the case of the positive shear tokamak [38]. The growth rate of the helical ITG mode is always smaller than that of the corresponding tokamak ITG mode. They are both significantly reduced for $\theta_k \to \pi/2$ when the toroidal destabilization does not work well at the poloidal angle of the mode localization. For the parameters used here, the helical ITG mode structure has a similar width along the field line to that of the tokamak ITG mode, and therefore the poloidal mode shift due to the θ_k-variation affects the stability more effectively than the α-variation as shown in the next subsection.

4.3.5 Effects of the field line label α

The non-axisymmetry of the helical system causes the α-dependence of the linear mode properties. We vary α within a toroidal period $-\pi/M < \alpha < \pi/M$ ($M = 10$). Figure 4.8 shows the normalized real frequency and growth rate as a function of α. The parameters used here are the same as the standard ones (see the first paragraph of this section) except

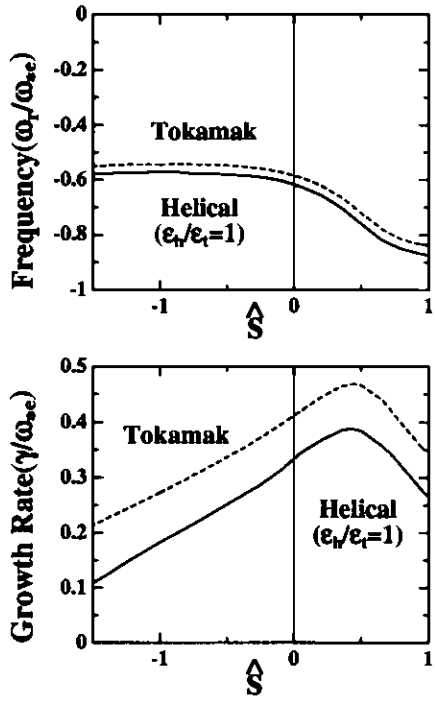

Figure 4.5: Normalized real frequency ω_r/ω_{*e} (top) and growth rate γ/ω_{*e} (bottom) as a function of the magnetic shear parameter $\hat{s}$ for $L = 2$, $M = 10$, $q = 2$, $\epsilon_h/\epsilon_t = 1$, $\theta_k = 0$, $\alpha = 0$, $\eta_i = 3$, $\epsilon_n = 0.3$, and $k_\theta \rho_{Ti} = 0.65$. The negative shear tokamak case with the same parameters except for $\epsilon_h/\epsilon_t = 0$ is plotted by the dotted line.

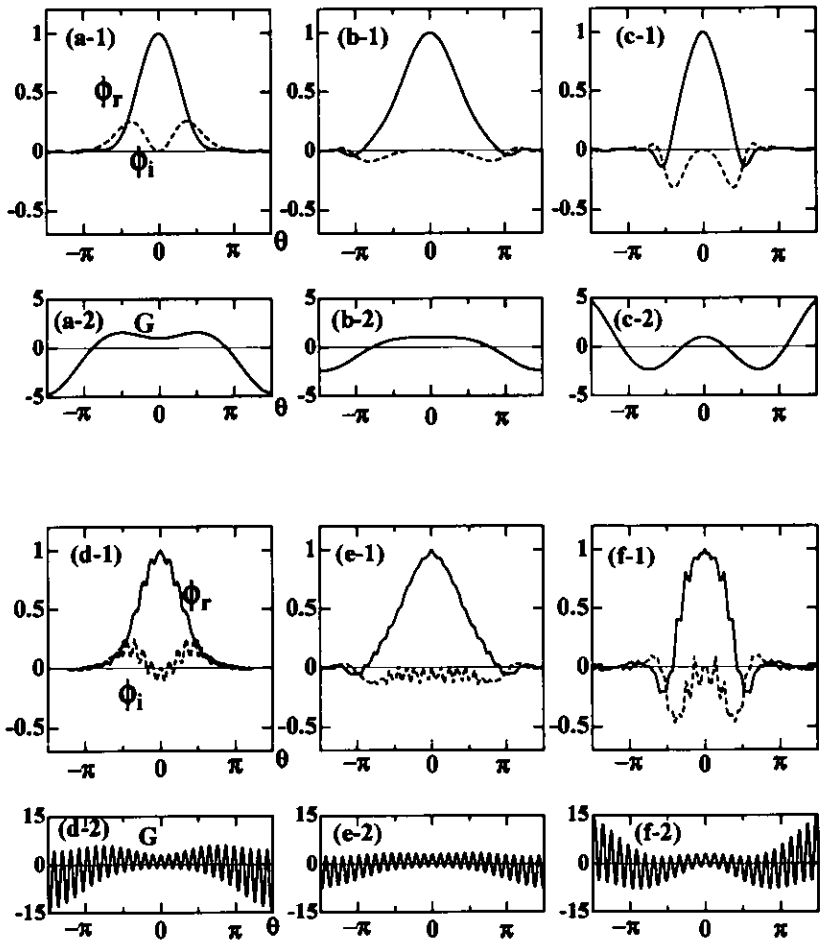

Figure 4.6: Eigenfunction $\phi(\theta) = \phi_r + i\phi_i$ and curvature factor $G(\theta)$ for the tokamak cases $\epsilon_h/\epsilon_t = 0$ with $\hat{s} = 1$ (a-1, 2), $\hat{s} = 0.5$ (b-1, 2), $\hat{s} = -1$ (c-1, 2), and for the helical cases $\epsilon_h/\epsilon_t = 1$ with $\hat{s} = 1$ (d-1, 2), $\hat{s} = 0.5$ (e-1, 2), $\hat{s} = -1$ (e-1, 2). The other parameters used here are $L = 2$, $M = 10$, $q = 2$, $\theta_k = 0$, $\alpha = 0$, $\eta_i = 3$, $\epsilon_n = 0.3$, and $k_\theta \rho_{Ti} = 0.65$.

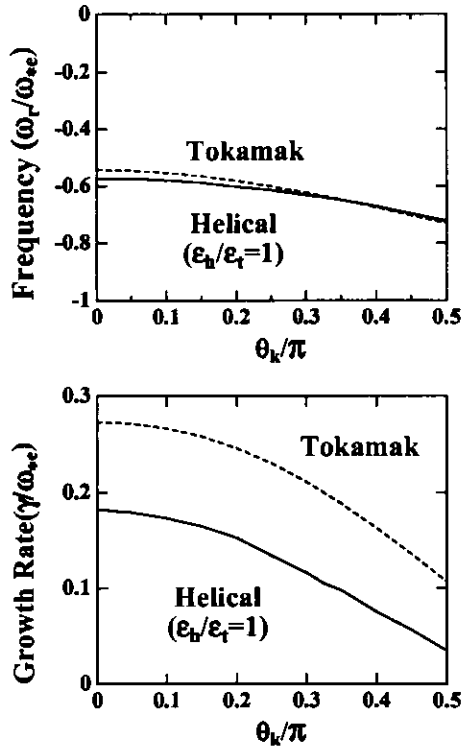

Figure 4.7: Normalized real frequency ω_r/ω_{*e} (top) and growth rate γ/ω_{*e} (bottom) as a function of θ_k for $L = 2$, $M = 10$, $q = 2$, $\hat{s} = -1$, $\epsilon_h/\epsilon_t = 1$, $\alpha = 0$, $\eta_i = 3$, $\epsilon_n = 0.3$, and $k_\theta \rho_{Ti} = 0.65$. The negative shear tokamak case with the same parameters except for $\epsilon_h/\epsilon_t = 0$ is plotted by the dotted line.

for α. We find that there is little dependence of the real frequency and growth rate on α. The curvature factor $G(\theta)$ is shown for $\alpha = 0, \pi/20$, and $\pi/10$ in Fig. 4.9. The weak α-dependence shown in Fig. 4.8 is interpreted as follows. In our model of the magnetic field strength, eq. (3.1), variation of α is reflected in the helical ripple phase shift. Since the ITG mode for the standard parameters extends in the whole region of the torus outside ($-\pi/2 < \theta < \pi/2$) like for the tokamak case, the small helical phase shift ($< 2\pi/M$) caused by varying α changes little the average effect of the helical ripples on the mode stability as expected from Fig. 4.9. However, we should note that our magnetic field model is valid only for low β values and that high β effects such as the Shafranov shift are not treated in it. If these high β effects are included, larger α-dependence may occur.

4.3.6 Dependence on the poloidal wavenumber

Figure 4.10 shows the normalized real frequency $\omega_r k_\theta \rho_{Ti}/\omega_{*e}$ and the normalized growth rate $\gamma k_\theta \rho_{Ti}/\omega_{*e}$ of the helical ITG mode as a function of the normalized poloidal wavenumber $k_\theta \rho_{Ti}$. Here, we employ $\omega_{*e}(k_\theta \rho_{Ti})^{-1}$ as the normalization unit for the frequency in order to remove the wavenumber dependence from the unit. For the LHD case mentioned earlier, we obtain $\omega_{*e}(k_\theta \rho_{Ti})^{-1} = 2.77 \times 10^5 sec^{-1}$. The parameters used here are the same as the standard ones (see the first paragraph of this section) except for $k_\theta \rho_{Ti}$. With increasing $k_\theta \rho_{Ti}$, the real frequency keeps its negative sign (the ion diamagnetic rotation) and its absolute value increases monotonically. We find the lower and upper boundaries in the poloidal wavenumber region for unstable modes ($\gamma > 0$). The maximum of the growth rate is given around $k_\theta \rho_{Ti} \simeq 0.65$, and this is why this poloidal wavenumber is taken as the standard one for the calculations in the previous subsections. The stable modes, which exist in the low and high poloidal wavenumber regions, are considered to play the role of the energy sink, which is necessary for the nonlinear saturation of the ITG modes.

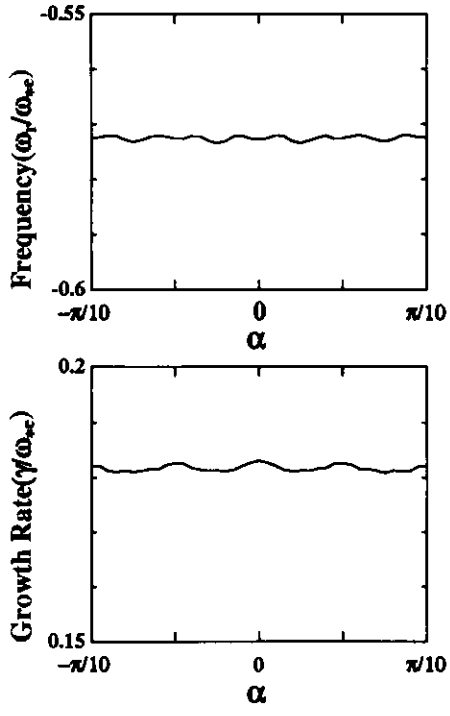

Figure 4.8: Normalized real frequency ω_r/ω_{*e} (top) and growth rate γ/ω_{*e} (bottom) as a function of the field line label α for $L = 2$, $M = 10$, $q = 2$, $\hat{s} = -1$, $\epsilon_h/\epsilon_t = 1$, $\theta_k = 0$, $\eta_i = 3$, $\epsilon_n = 0.3$, and $k_\theta \rho_{Ti} = 0.65$.

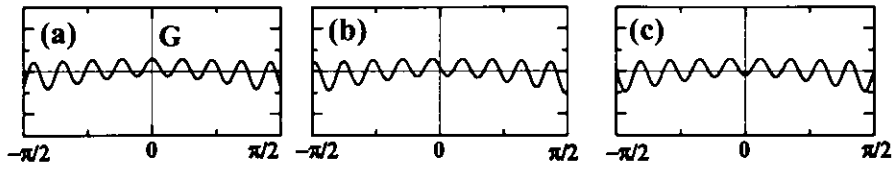

Figure 4.9: Curvature factor $G(\theta)$ for $\alpha = 0$ (a), $\alpha = \pi/20$ (b), and $\alpha = \pi/10$ (c). For these values of α, the phases of $G(\theta = 0)$ are different although the connection lengths between adjacent good and bad curvature regions are almost the same. The other parameters used here are $L = 2$, $M = 10$, $\epsilon_h/\epsilon_t = 1$, $q = 2$, $\hat{s} = -1$, $\theta_k = 0$, $\alpha = 0$, $\eta_i = 3$, $\epsilon_n = 0.3$, and $k_\theta \rho_{Ti} = 0.65$.

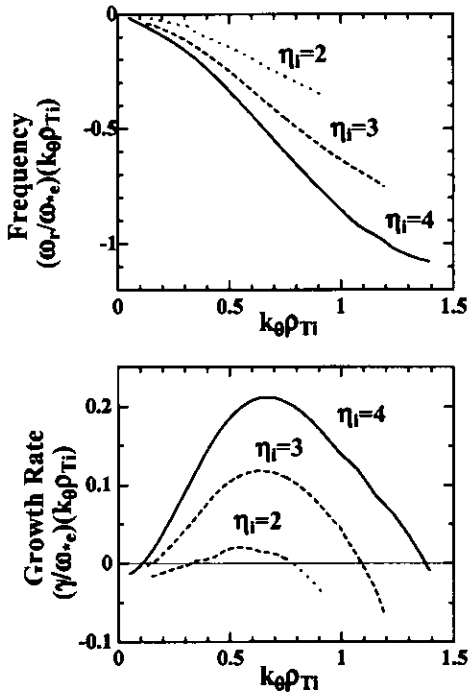

Figure 4.10: Normalized real frequency $k_\theta\rho_{Ti}\omega_r/\omega_{*e}$ (top) and growth rate $k_\theta\rho_{Ti}\gamma/\omega_{*e}$ (bottom) as a function of the normalized poloidal wavenumber $k_\theta\rho_{Ti}$ for $L = 2$, $M = 10$, $q = 2$, $\hat{s} = -1$, $\epsilon_h/\epsilon_t = 1$, $\theta_k = 0$, $\alpha = 0$, $\eta_i = 2, 3, 4$, and $\epsilon_n = 0.3$.

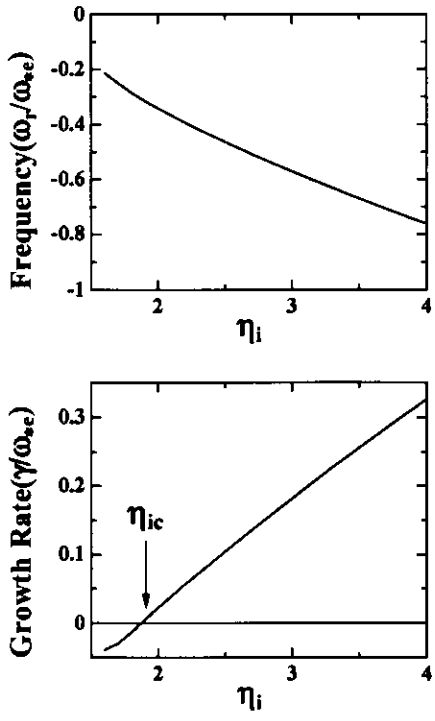

Figure 4.11: Normalized real frequency ω_r/ω_{*e} (top) and growth rate γ/ω_{*e} (bottom) as a function of η_i for $L = 2$, $M = 10$, $q = 2$, $\hat{s} = -1$, $\epsilon_h/\epsilon_t = 1$, $\theta_k = 0$, $\alpha = 0$, $\epsilon_n = 0.3$, and $k_\theta \rho_{Ti} = 0.65$.

4.3.7 Temperature gradient effects

Figure 4.11 shows the normalized real frequency ω_r/ω_{*e} and growth rate γ/ω_{*e} as a function of η_i. The parameters used here are the same as the standard ones (see the first paragraph of this section) except for η_i. As η_i increases, both the growth rate and the absolute value of the real frequency increase monotonically. Since our numerical code can calculate both positive and negative growth rates by proper analytic continuation of the dispersion relation, we can clearly identify the critical η_i value η_{ic} for which the growth rate vanishes.

4.3.8 Density gradient effects

Let us recall that the parameter $\epsilon_n = L_n/R = -n_0/(R\, dn_0/dr)$ is inversely proportional to the density gradient. Thus, we investigate the density gradient dependence of the ITG mode properties by varying ϵ_n. Hollow density profiles are often observed in helical systems [14]. Then, there exists a core plasma region, in which $dn/dr > 0$ and accordingly $\epsilon_n < 0$. Here, both cases with positive and negative ϵ_n are considered. Since the density gradient also appears in the definition of $\eta_i = L_n/L_{Ti}$, we impose the constraint $\eta_i/\epsilon_n = R/L_{Ti} = 10$ to fix the temperature gradient. This constraint $\eta_i/\epsilon_n = R/L_{Ti} = 10$ is chosen since it is given for the case of the standard parameters. The parameters used here are the same as the standard ones (see the first paragraph of this section) except for ϵ_n and η_i. The density gradient effects are shown in Fig. 4.12, where the normalized real frequency $\omega_r/(\omega_{*e}\epsilon_n)$ and the normalized growth rate $\gamma/(\omega_{*e}\epsilon_n)$ are shown as a function of ϵ_n. Here, we employ the new normalization unit $\omega_{*e}\epsilon_n$ in order to remove the density gradient dependence from the unit. We should note that the ϵ_n variation from $\epsilon_n = +0$ (-0) to $\epsilon_n = +\infty$ $(-\infty)$ corresponds to the density gradient variation from $dn_0/dr = -\infty$ $(+\infty)$ to $dn_0/dr = -0$ $(+0)$. The growth rate has a peak at the negative density gradient with $\epsilon_n = 0.2$. For more flattened negative density gradient ($\epsilon_n > 0.2$), the growth rate becomes smaller. Furthermore, increasing the density gradient from $dn_0/dr = +0$ to $+\infty$, the growth rate continues to decrease. Similar ϵ_n-dependence of the real frequency is found although it has no peak in the region $\epsilon_n > 0$. The hollow density profile is considered to be more stable against the ITG mode than the normal profile with the same temperature gradient.

4.4 Conclusions

In this chapter, we have investigated the linear ITG modes in helical systems. Using the ion gyrokinetic equation, the adiabatic electron assumption, and the quasineutrality condition, the ITG mode dispersion relation is derived as an integral equation, where effects of

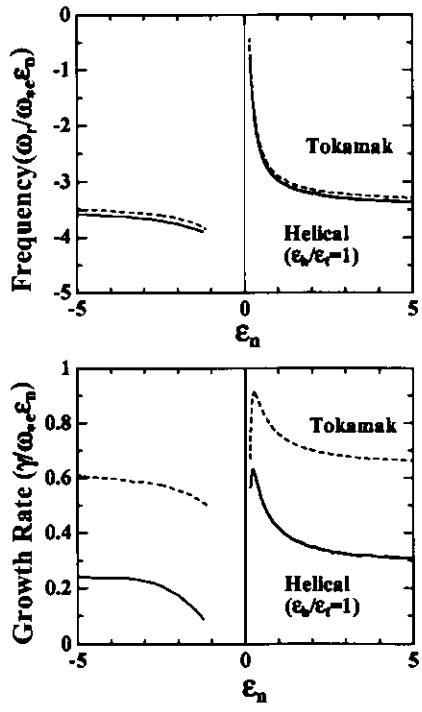

Figure 4.12: Normalized real frequency $\omega_r/(\omega_{*e}\epsilon_n)$ (top) and growth rate $\gamma/(\omega_{*e}\epsilon_n)$ (bottom) as a function of ϵ_n under the constraint $\eta_i/\epsilon_n = -[T_i^{-1}dT_i/dr]R = 10$ for $L = 2$, $M = 10$, $q = 2$, $\hat{s} = -1$, $\epsilon_h/\epsilon_t = 1$, $\theta_k = 0$, $\alpha = 0$, and $k_\theta \rho_{Ti} = 0.65$. The negative shear tokamak case with the same parameters except for $\epsilon_h/\epsilon_t = 0$ is plotted by the dotted line. Here, the ϵ_n variation from $\epsilon_n = +0$ (-0) to $\epsilon_n = +\infty$ $(-\infty)$ corresponds to the density gradient variation from $dn_0/dr = -\infty$ $(+\infty)$ to $dn_0/dr = -0$ $(+0)$.

toroidal and helical magnetic ripples are taken into account through the ion ∇B-curvature drift frequency. By numerically solving the integral equation with the proper analytic continuation performed, the real frequency, growth rate, and eigenfunction are obtained for both stable and unstable cases. The numerical results have shown dependences of these linear ITG mode properties on various parameters including the helical ripple intensity, safety factor, magnetic shear, ballooning angle, poloidal wavenumber, temperature and density gradients. Typical parameter values used here are given by considering the LHD experiment. Also, the characteristics of the ITG mode in the helical system are compared with those for the tokamak case with the same parameters except for no helical ripples.

Due to the helical ripples, the connection lengths between adjacent good and bad curvature regions are reduced, and the good curvature regions also appear even in the outside of the torus. Then, the ITG modes for the case of finite helical ripples are more stable than for the corresponding tokamak case. The eigenfunctions for the helical case spread in the whole torus outside region like those for the tokamak case, although the former are rippled by the helical magnetic structure. For both tokamak and helical cases, the negative magnetic shear reduces the bad curvature region and accordingly the growth rate.

The field line label effects are not so obvious as the stabilizing effects of varying the ballooning angle parameter. Stronger dependence on the field line label may happen if we consider other effects such as the Shafranov shift which are not included in our magnetic field model here. In order to treat this problem more accurately, more detailed magnetic field model should be used. Also, effects of nonadiabatic electrons, trapped ions, collisions, impurities, and sheared radial electric fields, which are not treated in this work, remain as future problems.

Chapter 5

Conclusions

In this thesis, gyrokinetic analysis have been done on the ion temperature gradient (ITG) modes in toroidal systems. Results obtained in this thesis are summarized as follows.

It is found in the local approximation that, for the toroidal ITG mode, temporal dependence of the density and potential perturbations is described by two types of behavior. One is well-known normal modes which change exponentially in time. Their frequencies and growth rates are determined by the dispersion relation and correspond to the poles of the Laplace-transformed potential function on the complex frequency plane. The other is a continuum mode which is given by the integration of the Laplace-transformed potential function along a branch cut. Occurrence of the branch cut is due to the quadratic velocity dependence of the toroidal ∇B-curvature drift. The long-time asymptotic behavior of the continuum mode is characterized by oscillation at the branch frequency and power law decay $\propto t^{-3/2}$. This behavior is the same as that of the ballistic response obtained by the propagator of the gyrokinetic equation without taking account of interaction with the potential.

If the normal mode analysis shows the system to be unstable, the long-time behavior is dominantly described by the normal mode with the largest growth rate. On the other hand, when the system is stable, only the normal modes are not enough for describing the

temporal evolution of the toroidal ITG mode. In the stable case, the system is eventually dominated by the continuum mode since all the normal modes decay more rapidly.

We have also investigated the linear ITG modes in straight and toroidal helical systems. Using the ion gyrokinetic equation, the adiabatic electron assumption, and the quasineutrality condition, the ITG mode dispersion relation is derived as an integral equation, where effects of toroidicity and helical magnetic ripples are taken into account through the ion ∇B-curvature drift frequency. By numerically solving the integral equation with the proper analytic continuation performed, the real frequency, growth rate, and eigenfunction are obtained for both stable and unstable cases.

For a straight helical system with the poloidal polarity number $L = 2$, the effects of the toroidal polarity number M on the dispersion relation and the mode structure of the ITG mode were studied. Field ripple with larger M reduces the growth rate of the ITG mode. This stabilizing effect is understood based on the structure of the eigenfunction along the field line as follows. As M increases, the connection length between the good and bad curvature regions becomes shorter and the eigenfunction enters the good curvature region, which leads to the stabilization.

The numerical results for the case of toroidal helical systems have shown dependences of these linear ITG mode properties on various parameters including the helical ripple intensity, safety factor, magnetic shear, ballooning angle, poloidal wavenumber, temperature and density gradients. Because of the toroidal destabilization, the critical temperature gradient in which ITG mode becomes unstable is smaller than for the straight helical system. Typical parameter values used here are given by considering the LHD experiment. Numerical results suggest the existence of unstable ITG modes in LHD ($\lambda_\theta = 2.0$ cm, $\omega_r \simeq -0.97 \times 10^5$ [sec]$^{-1}$, $\gamma \simeq 0.33 \times 10^5$ [sec]$^{-1}$). From the mixing length argument, the diffusion coefficient is estimated by $D \sim \gamma/k_\theta^2 \simeq 0.35$[m^{2}sec^{-1}] for the LHD parameters used here.

Also, the characteristics of the ITG mode in the helical system are compared with those

for the tokamak case with the same parameters except for no helical ripples. Due to the helical ripples, the connection lengths between adjacent good and bad curvature regions are reduced, and the good curvature regions also appear even in the outside of the torus. Then, the ITG modes for the case of finite helical ripples are more stable than for the corresponding tokamak case. The eigenfunctions for the helical case spread in the whole torus outside region like those for the tokamak case, although the former are rippled by the helical magnetic structure. For both tokamak and helical cases, the negative magnetic shear reduces the bad curvature region and accordingly the growth rate.

The field line label effects are not so obvious as the stabilizing effects of varying the ballooning angle parameter. Stronger dependence on the field line label may happen if we consider other effects such as the Shafranov shift which are not included in our magnetic field model here. In order to treat this problem more accurately, more detailed magnetic field model should be used. Also, effects of nonadiabatic electrons, trapped ions, collisions, impurities, and sheared electric fields, which are not treated in this work, remain as future problems. However, we believe that the results obtained here give the basics of further studies on microinstabilities in helical systems.

Acknowledgements

It is a great pleasure to thank many people who made this thesis possible. First of all, I am grateful to my supervisor, Prof. M. Okamoto, whose elaborate guidance and advice in conversation and in discussion benefit me throughout my doctor course. I would like to express my special gratitude to Dr. H. Sugama, for his continuous encouragement with generosity and advice based on the remarkable understanding in physics throughout this entire work. He taught me the physics of toroidal plasmas from the basic subjects to the applications. I appreciate kindness of Dr. R. Kanno who gave me fruitful suggestions and cooperation on this work. Dr. Y. Kishimoto gave me useful comments which brought profound comprehension on physics concerned with this work of Chapter 2. It is joyful for me to have enjoyed the collaboration with Prof. W. Horton in the work of Chapter 2. I would like to acknowledge the helpful comment by Dr. G. Rewoldt on the work in Chapter 3. My appreciation is extended to Dr. N. Nakajima and Dr. M. Yokoyama for their useful advice and discussion, to Dr. S. Murakami who often helped me solve troubles on computers, to Dr. K. Ichiguchi whose lecture on plasma physics enlightened me, and to Dr. R. Ishizaki whose advice was always useful when I was in trouble with research activities. I am very grateful to all staff members of Theory and Data Analysis Division of NIFS. I am thankful to Prof. K. Yamazaki and Dr. H. Yamada for communications of the experimental data on LHD.

I am also grateful to students at NIFS, especially to Dr. K. Orito who gave me a large amount of knowledge on computers. Lastly, I would like to express my gratitude to the friendship and the encouragement of Mr. T. Kobuchi, Mr. T. Kondo, Mr. Y. Shirai, Mr. K. Hirose, Mr. K. Matsushita and Mr. N. Mizuguchi, which supported my days in the Graduate University for Advanced Studies.

References

[1] J. P. Freidberg: *Ideal Magnetohydrodynamics*, Plenum Press, New York (1987).

[2] S. I. Braginskii: *Transport process in a plasma*, Rev. Plasma Phys., Consultants Bureau, New York, (1965).

[3] F. L. Hinton and R. D. Hazeltine: Rev. Mod. Phys. **42** (1976) 239.

[4] S. P. Hirshman and D. J. Sigmar: Nucl. Fusion **21** (1981) 1079.

[5] R. Balescu: *Transport Process in Plasmas*, **1** and **2**, North-Holland, Amsterdam (1988).

[6] J. B. Taylor and H. R. Wilson: Plasma Phys. Control. Fusion **38** (1996) 1999.

[7] W. Horton: Rev. Mod. Phys. **71** (1999) 735.

[8] W. Horton, M. Wakatani, and J. A. Wooton: *AIP Conference Proceedings 284, U.S.-Japan Workshop on Ion Temperature Gradient-Driven Turbulent Transport*, New York: AIP, 1994, ch. 1, p. 3.

[9] J. Y. Kim and W. Horton: Phys. Fluids B **3** (1991) 1167.

[10] A. Iiyoshi, M. Fujiwara, O. Motojima, N. Ohyabu, and K. Yamazaki: Fusion Technol. **17** (1990) 169.

[11] M. Fujiwara, K. Yamazaki, M. Okamoto, J. Todoroki, T. Amano, T. Watanabe, T. Hayashi, H. Sanuki, N. Nakajima, K. Itoh, H. Sugama, K. Ichiguchi, S. Murakami,

O. Motojima, J. Yamamoto, T. Satow, N. Yanagi, S. Imagawa, K. Takahata, H. Tamura, A. Nishimura, A. Komori, N. Inoue, N. Noda, A. Sagara, Y. Kubota, N. Akaishi, S. Satoh, S. Tanahashi, H. Chikaraishi, T. Mito, S. Yamada, S. Yamaguchi, S. Sudo, K. N. Sato, T. Watari, T. Kuroda, O. Kaneko, K. Ohkubo, S. Kitagawa, A. Ando, H. Idei, K. Tsumori, S. Kubo, R. Kumazawa, T. Mutoh, Y. Oka, M. Sato, T. Seki, T. Shimozuma, Y. Takeiri, Y. Hamada, K. Narihara, K. Kawahata, S. Fujisawa, S. Hidekuma, T. Minami, I. Yamada, A. Ejiri, K. Tanaka, M. Sasao, H. Iguchi, K. Y. Watanabe, H. Yamada, N. Ohyabu, H. Suzuki, and A. Iiyoshi: J. Fusion Energy **15** (1996) 7.

[12] M. Fujiwara, O. Motojima, Y. Hamada, T. Watari, M. Okamoto, J. Yamamoto, T. Kuroda, the LHD Group and A. Iiyoshi: Plasma Phys. Control. Fusion **39** (1997) 261.

[13] A. Iiyoshi, A. Komori, A. Ejiri, M. Emoto, H. Funaba, M. Goto, K. Ida, H. Idei, S. Inagaki, S. Kado, O. Kaneko, K. Kawahata, T. Kobuchi, S. Kubo, R. Kumazawa, S. Masuzaki, T. Minami, J. Miyazawa, T. Morisaki, S. Morita, S. Murakami, S. Muto, T. Mutoh, Y. Nagayama, Y. Nakamura, H. Nakanishi, K. Narihara, K. Nishimura, N. Noda, S. Ohdachi, N. Ohyabu, Y. Oka, M. Osakabe, T. Ozaki, B. J. Petereson, A. Sagara, S. Sakakibara, R. Sakamoto, H. Sasao, M. Sasao, K. Sato, M. Sato, T. Seki, T. Shimozuma, M. Shoji, H. Suzuki, Y. Takeiri, K. Tanaka, K. Toi, T. Tokuzawa, K. Tsumori, K. Tsuzuki, K. Y. Watanabe, T. Watari, H. Yamada, I. Yamada, S. Yamaguchi, M. Yokoyama, R. Akiyama, H. Chikaraishi, K. Haba. S. Hamaguchi, M. Iima, S. Imagawa, N. Inoue, K. Iwamoto, S. Kitagawa, J. Kodaira, Y. Kubota, R. Maekawa, T. Mito, T. Nagasaka, A. Nishimura, C. Takahashi, K. Takahata, Y. Takita, H. Tamura, T. Tsuzuki, S. Yamada, K. Yamauchi, N. Yanagi, H. Yonezu, Y. Hamada, K. Matsuoka, K. Murai, K. Ohkubo, I. Ohtake, M. Okamoto, S. Satoh, T. Satow, S. Sudo, S. Tanahashi, K. Yamazaki, M. Fujiwara, and O. Motojima: Nucl. Fusion **39** (1999).

[14] M. Fujiwara, H. Yamada, A. Ejiri, M. Emoto, H. Funaba, M. Goto, K. Ida, H. Idei,

S. Inagaki, S. Kado, O. Kaneko, K. Kawahata, T. Kobuchi, A. Komori, S. Kubo, R. Kumazawa, S. Masuzaki, T. Minami, J. Miyazawa, T. Morisaki, S. Morita, S. Murakami, S. Muto, T. Mutoh, Y. Nagayama, Y. Nakamura, H. Nakanishi, K. Narihara, K. Nishimura, N. Noda, S. Ohdachi, N. Ohyabu, Y. Oka, M. Osakabe, T. Ozaki, B. J. Peterson, A. Sagara, S. Sakakibara, R. Sakamoto, H. Sasao, M. Sasao, K. Sato, M. Sato, T. Seki, T. Shimozuma, M. Shoji, H. Suzuki, Y. Takeiri, K. Tanaka, K. Toi, T. Tokuzawa, K. Tsumori, K. Tsuzuki, K.Y. Watanabe, T. Watari, I. Yamada, S. Yamaguchi, M. Yokoyama, R. Akiyama, H. Chikaraishi, K. Haba, S. Hamaguchi, M. Iima, S. Imagawa, N. Inoue, K. Iwamoto, S. Kitagawa, J. Kodaira, Y. Kubota, R. Maekawa, T. Mito, T. Nagasaka, A. Nishimura, C. Takahashi, K. Takahata, Y. Takita, H. Tamura, T. Tsuzuki, S. Yamada, K. Yamauchi, N. Yanagi, H. Yonezu, Y. Hamada, K. Matsuoka, K. Murai, K. Ohkubo, I. Ohtake, M. Okamoto, S. Satoh, T. Satow, S. Sudo, S. Tanahashi, K. Yamazaki, O. Motojima, A. Iiyoshi: Nucl. Fusion **39** (1999) 1659.

[15] N. Ohyabu,*et al.*: to be published in Journal of Plasma and Fusion Research [in Japanese].

[16] J. Q. Dong, W. Horton, and J. Y. Kim: Phys. Fluids B **4** (1992) 1867.

[17] L. I. Rudakov and R. Z. Sagdeev: Sov. Phys.-Dokl. **6** (1961) 415.

[18] J. Y. Kim and M. Wakatani: Phys. Plasmas **2** (1995) 1012.

[19] W. Horton and R. K. Varma: Phys. Fluids **15** (1972) 620.

[20] C. Z. Cheng and K. T. Tsang: Nucl. Fusion **21** (1981) 643.

[21] F. Romanelli: Phys. Fluids B **1** (1989) 1018.

[22] G. W. Hammett, M. A. Beer, W. Dorland, S. C. Cowley, and S. A. Smith: Plasma Phys. Control. Fusion **35** (1993) 973.

[23] M. A. Beer and G. W. Hammett: Phys. Plasmas **3** (1996) 4046.

[24] G. Rewoldt and W. M. Tang: Phys. Fluids B **2** (1990) 318.

[25] M. Kotschenreuther, G. Rewoldt and W. M. Tang: Comput. Phys. Commun. **88** (1995) 128.

[26] P. H. Rutherford and E. A. Frieman: Phys. Fluids **11** (1968) 569.

[27] J. B. Taylor and R. J. Hastie: Plasma Phys. **10** (1968) 479 .

[28] P. Similon, J. E. Sedlak, D. Stotler, H. L. Berk, W. Horton, and D. Choi: J. Comput. Phys. **54** (1984) 260.

[29] J. Y. Kim, Y. Kishimoto, W. Horton, and T. Tajima: Phys. Plasmas **1** (1994) 927.

[30] T. Kuroda, H. Sugama, R. Kanno, M. Okamoto, and W. Horton, J. Phys. Soc. Jpn. **67** (1998) 3787.

[31] N. Nishimura, *et al.*: Fusion Technol. **17** (1990) 86.

[32] J. L. V. Lewandowski: Plasma Phys. Control. Fusion **40** (1998) 283.

[33] T. Kuroda, H. Sugama, R. Kanno, and M. Okamoto: Journal of Plasma and Fusion Research SERIES, **2** (1999) 105.

[34] R. D. Hazeltine and J. D. Meiss: *Plasma Confinement* (Addison-Wesley, Redwood City, CA, 1992) p.298.

[35] R. L. Dewar and A. H. Glasser: Phys. Fluids **26** (1983) 3038.

[36] G. Rewoldt, L.-P. Ku, W. M. Tang, and W. A. Cooper: Phys. Plasmas **6** (1999) 4705.

[37] T. Kuroda, H. Sugama, R. Kanno, and M. Okamoto: submitted to J. Phys. Soc. Jpn.

[38] H. Sugama: Phys. Plasmas **6** (1999) 3527.

[39] J. Q. Dong, Y. Z. Zhang, S. M. Mahajan, and P. N. Guzdar: Phys. Plasmas **3** (1996) 3065.

[40] W. A. Cooper: Plasma Phys. control. Fusion **30** (1988) 1805.

[41] H. Sugama and W. Horton: in *Two-dimensional Turbulence in Plasmas and Fluids*, edited by R. L. Dewar and R. W. Griffiths (American Institute of Physics, New York, 1997), p. 275.

[42] G. Rewoldt, L. L. Lao, and W. M. Tang: Phys. Plasmas **4** (1997) 3293.